ABSTRACT

SCANLESS OPTICAL COHERENCE TOMOGRAPHY FOR HIGH-SPEED 3D BIOMEDICAL MICROSCOPY

by
Yahui Wang

Optical coherence tomography (OCT) is a high-resolution cross-sectional imaging modality that has found applications in a wide range of biomedical fields, such as ophthalmology diagnosis, interventional cardiology, surgical guidance, and oncology. OCT can be used to image dynamic scenes, in quantitative blood flow sensing and visualization, dynamic optical coherence elastography, and large-scale neural recording. However, the spatiotemporal resolution of OCT for dynamic imaging is limited by the approach it takes to scan the three-dimensional (3-D) space. In a typical OCT system, the incident light is focused to a point at the sample. The OCT system uses mechanical scanners (galvanometers or MEMS scanners) steer the probing beam to scan the transverse plane and acquires an A-scan at each transverse coordinate. For volumetric imaging, the OCT system scans individual voxels in a 3D Cartesian coordinate sequentially, resulting a limited imaging speed. In addition to limited spatiotemporal resolution, the use of mechanical scanners results in bulky sample arm and complex system configuration.

This dissertation seeks to overcome limitations of conventional raster scanning approach for OCT data acquisition, by investigating novel methods to address OCT voxels in 3D space. Scanless OCT imaging is achieved through the use of spatial light modulator that precisely manipulates light wave to generate output with desired amplitude and phase. It is anticipated that the scanless OCT imaging technologies developed in this dissertation will introduce a significant paradigm shift in OCT scanning of 3D space and allow the observation of transient phenomena (neural activities, blood flow dynamics, etc.) with unprecedented spatiotemporal resolution.

This research focuses on technology development and validation. Two approaches for scanless OCT imaging are investigated. One approach is optically computed optical coherence tomography (OC-OCT), and the other approach is Line field Fourier domain OCT (LF-FDOCT) based on spatial light modulator. OC-OCT takes a highly innovative optical computation strategy to extract signal from a specific depth directly without signal processing in a computer. The optical computation module in OC-OCT performs Fourier transform optically before data acquisition, by calculating the inner product between a Fourier basis function projected by the spatial light modulator and the Fourier domain interferometric signal. OC-OCT allows phase resolved volumetric OCT imaging without mechanical scanning, and has the capability to image an arbitrary 2D plane in a snapshot manner. LF-FDOCT illuminates the sample with a line field generated by a spatial light modulator. Interferometric signals from different transverse coordinates along the line field are dispersed by a grating and detected in parallel by the rows of a 2D camera. Cross-sectional image (Bscan) is obtained by performing Fourier transform along the rows of the camera. By scanning the line field electronically at the SLM, volumetric OCT imaging can be performed without mechanical scanning.

In this dissertation, the principles of OC-OCT and LF-FDOCT technology are described. The imaging capability of OC-OCT and LF-FDOCT systems are quantitatively evaluated and demonstrated in 2D and 3D imaging experiments on a variety of samples.

SCANLESS OPTICAL COHERENCE TOMOGRAPHY FOR HIGH-SPEED 3D BIOMEDICAL MICROSCOPY

by
Yahui Wang

A Dissertation
Submitted to the Faculty of
New Jersey Institute of Technology
in Partial Fulfillment of the Requirements for the Degree of
Doctor of Philosophy in Electrical Engineering

Helen and John C. Hartmann
Department of Electrical and Computer Engineering

May 2020

.

APPROVAL PAGE

SCANLESS OPTICAL COHERENCE TOMOGRAPHY FOR HIGH-SPEED 3D BIOMEDICAL MICROSCOPY

Yahui Wang

Dr. Xuan Liu, Dissertation Advisor Date
Assistant Professor of Electrical and Computer Engineering, NJIT

Dr. Haim Grebel, Committee Member Date
Professor of Electrical and Computer Engineering, NJIT

Dr. Bryan J. Pfister, Committee Member Date
Professor of Biomedical Engineering, NJIT

Dr. Yuanwei Zhang, Committee Member Date
Assistant Professor of Chemical and Materials Engineering, NJIT

Dr. Nguyen, Hieu Pham Trung, Committee Member Date
Assistant Professor of Electrical and Computer Engineering, NJIT

BIOGRAPHICAL SKETCH

Author: Yahui Wang

Degree: Doctor of Philosophy

Date: May 2020

Undergraduate and Graduate Education:

- Doctor of Philosophy in Electrical Engineering,
  New Jersey Institute of Technology, Newark, NJ, USA, 2020

- Master of Science in Electrical Engineering,
  New Jersey Institute of Technology, Newark, NJ, USA, 2016

- Bachelor of Science in Electrical and Electronic Engineering,
  Dalian Maritime University, Liaoning, China, 2014

Major: Electrical Engineering

Presentations and Publications:

Journal Articles:

Y. Wang and X. Liu “Line field Fourier domain OCT based on a spatial light modulator,” (to be submitted)

Y. Wang, Q. Kang, Y. Zhang, and X. Liu, “Optically computed optical coherence tomography for volumetric imaging,” *Optics Letters,* 2020.

Y. Qiu, Y. Wang, Y. Xu, N. Chandra, J. Haorah, B. Hubbi, B. J. Pfister,and X. Liu, “Quantitative optical coherence elastography based on fiber-optic probe for in situ measurement of tissue mechanical properties,”Biomedical *Optics Express*, vol. 7, no. 2, pp. 688–700, 2016.

Y. Wang, Y. Wang, A. Akansu, K. Belfield, B. Hubbi, and X. Liu, "Robust motion tracking based on adaptive speckle decorrelation analysis of OCT signal," Biomed. *Optics. Express* 6, 4302-4316, 2015.

X. Liu, F. R. Zaki, and Y. Wang, “Quantitative optical coherence elastography for robust stiffness assessment,” *Applied Science*, vol. 8, no. 8, pp. 1255, 2018.

X. Liu, F. R. Zaki, H. Wu, C. Wang, and Y. Wang, “Temporally and spatially adaptive Doppler analysis for robust handheld optical coherence elastography,” *Biomedical Optics Express*, vol. 9, no. 7, pp. 3335-3353, 2018.

F. R. Zaki, Y. Wang, H., X. Yuan, and X. Liu, “Noise adaptive wavelet thresholding for speckle noise removal in optical coherence tomography,” *Biomedical Optics Express*, vol. 8, no. 5, pp. 2720-2731, 2017.

X. Liu, F. R. Zaki, Y. Wang, Q. Huang, X., and J. Wang, “Secure fingerprint identification based on structural and microangiographic optical coherence tomography,” *Applied Optics*, vol. 56, no. 8, pp. 2255-2259, 2017.

Conference Papers:

F. R. Zaki, Y. Wang, C. Wang, and X. Liu, “Adaptive Doppler analysis for robust handheld optical coherence elastography,” In Proc. *SPIE* 10880, Optical Elastography and Tissue Biomechanics VI, 108801I, 21 February 2019.

F. R. Zaki, Y. Wang, X. Yuan, and X. Liu, “Adaptive wavelet thresholding for optical coherence tomography image denoising,” in *Imaging and Applied Optics* 2017 (3D, AIO, COSI, IS, MATH, pcAOP), OSA Technical Digest (online), Optical Society of America, 2017, paper CTh4B.4.

X. Liu, F. R. Zaki, and Y. Wang, “Robust stiffness quantification using quantitative optical coherence elastography,” In *Conference on Lasers and Electro-Optics*, Optical Society of America, 2017.

Y. Wang and X. Liu, "Compressive OCT based on spectral domain random encoding," in *Conference on Lasers and Electro-Optics*, OSA Technical Digest (online) (Optical Society of America, 2018), paper JTu2A.108.

Y. Wang, Y. Qiu, F. R. Zaki, Y. Xu, B. Hubbi, K. D. Belfield, and X. Liu; “Entropy analysis of OCT signal for automatic tissue characterization,” In Proc. *SPIE* 9720, High-Speed Biomedical Imaging and Spectroscopy: Toward Big Data Instrumentation and Management, 972018, 7 March 2016.

Y. Qiu, F. R. Zaki, Y. Wang, Y. Xu, N. Chandra, J. Haorah, B. Hubbi, B. Pfister, and X. Liu, “Depth resolved optical coherence elastography based on fiber-optic probe with integrated Fabry-Perot force sensor,” In *Conference on Lasers and Electro-Optics,* OSA Technical Digest (online), Optical Society of America, 2016, paper AW1O.3.

Y. Qiu, Y. Wang, and X. Liu, "Ultrathin fiber optic probe for OCT imaging," in *Conference on Lasers and Electro-Optics*, OSA Technical Digest (online) (Optical Society of America, 2016), paper AW1O.5.

Y. Qiu, Y. Wang, Y. Xu, N. Chandra, J. Haorah, B. Hubbi, B. J. Pfister, and X. Liu "Quantitative optical coherence elastography based on fiber-optic probe with integrated Fabry-Perot force sensor", Proc. *SPIE* 9702, Optical Fibers and Sensors for Medical Diagnostics and Treatment Applications XVI, 97020W (7 March 2016); doi: 10.1117/12.2212917

Poster Presentations:

F. R. Zaki, Y. Wang, C. Wang, and X. Liu, "Adaptive doppler analysis for robust handheld optical coherence elastography," presented at *BiOS* Poster Presentation, *SPIE* Photonic West 2019, San Francisco, CA, 2019.

Y. Wang, Y. Qiu, F. R. Zaki, Y. Xu, B. Hubbi, K. D. Belfield, and X. Liu; "Entropy analysis of OCT signal for automatic tissue characterization," In Proc. *SPIE* 9720, High-Speed Biomedical Imaging and Spectroscopy: Toward Big Data Instrumentation and Management, 972018, 7 March 2016.

To my parents and my girlfriend,

who encouraged me a lot

ACKNOWLEDGMENT

At first, I would like to express my sincere and greatest gratitude to my dissertation advisor, Dr. Xuan Liu, for her continuous guidance, constant support, numerous patience and inspiring encouragement throughout my Ph.D. journey. She offered me the opportunity to begin my Ph.D. study and helped me enormously to enter the OCT medical imaging field. I have not only gained the knowledge about my research but also learnt professional communication skills from her. Her wisdom and diligence coupled with her experience makes her one of my most admired people. I could not have imagined having a better advisor and mentor for my Ph.D. study.

I also want to express my gratitude to all my dissertation committee members, Dr. Haim Grebel, Dr. Bryan J. Pfister, Dr. Yuanwei Zhang and Dr. Nguyen, Hieu Pham Trung for their valuable suggestions. During my Ph.D. coursework, I took the communication system and pattern recognition taught by Dr. Osvaldo Simeone. I am grateful to him to help me understand the concepts of communication theory and machine learning that inspired my experimental setup. I am also thankful to Dr. Yun Q. Shi who helped me to understand the basic fundamental concepts of image enhancement and image restoration techniques during my coursework of digital image processing that I have applied later during the signal processing of my experiments. I would also like to express my sincere gratitude to Dr. Ali N. Akansu who helped to understand the basics of signal processing and FPGA during my coursework of digital signal processing. I would like to thank Mr. Qi Kang of Brookhaven National Laboratory for his guidance and support to fabricate a 3D phantom by depositing photoresist using the photolithography facility and helpful discussions for this research.

In addition, I would like to thank my Ph.D. graduate advisor Dr. Durgamadhab Misra who encouraged and advised me for the last four years. I would like to express my gratitude to all our funding agencies (National Institute of Health (NIH), Provost scholarship from New Jersey Institute of Technology (NJIT) I would also like to thank ECE department of NJIT for all their supports throughout my entire Ph.D. journey. My appreciation also goes to Ms. Clarisa González-Lenahan, Dr. Sotirios G. Ziavras and the Office of Graduate Studies (GSO) of NJIT to provide me the valuable guidelines and assistance to format this dissertation.

I would like to thank my friend and my lab-mate Dr. Farzana Zaki and Dr. Yi Qiu for their enormous support in this journey. I am also thankful to my friends specially Xiaopeng Chen, Lei Zhao, TingTing Liu, Zhiyi Li, Yuwei Liu, Xingyu Zhou, Annan Dong, Anqi Xiong, Fu Rao to encourage me throughout this journey.

Last, but not least, I am thankful to my parents for their continuous inspiration, encouragement, support and guidance. Their beliefs have given me the courage to achieve my dreams. I would like to express my heartiest gratitude to my grandma Qingfang Wang and grandpa Shancheng Wang on my father’s side and my grandma Shumei Wang and grandpa Fugao Suo on my mother’s side for their support and encouragement throughout my journey.

TABLE OF CONTENTS

Chapter **Page**

TABLE OF CONTENTS
(Continued)

Chapter **Page**

LIST OF FIGURES

TABLE OF FIGURES
(Continued)

CHAPTER 1

INTRODUCTION

1.1 Background

Optical coherence tomography (OCT) is a high-resolution cross sectional imaging modality and has found applications in wide range of biomedical fields, such as ophthalmology, cardiology and oncology [6]. High-speed OCT imaging has been used in quantitative blood flow imaging, dynamic optical coherence elastography, and large-scale neural recording [36-38]. In conventional OCT imaging, the light beam is steered mechanically in the transverse plane to generate Bscan or Cscan images, and an Ascan is obtained at each transverse coordinate. Although on average it takes a very short time interval to acquire one OCT pixel [39], the raster beam scanning results in limited spatiotemporal resolution in OCT imaging. Particularly, it takes a long time to acquire a 2D imaging in any non-Bscan plane. For a conventional OCT imaging system that performs raster beam scanning in the Cartesian coordinate system, 2D image in a non-Bscan plane is achieved by capturing a complete 3D volume data cube and extract pixels within the plane to generate the image. However, high-speed OCT imaging in a certain dimension such as *en-face* plane is more desirable in many applications than the capability to perform 3D imaging at a low Cscan rate. The raster beam scanning also causes large inter-Bscan sampling interval and even larger inter-Cscan sampling interval. What's more, the use of a mechanical beam scanner such as a galvanometer or a micro-electromechanical system (MEMS) increases the dimension, cost and complexity of the sample arm for an OCT imaging system.

In order to acquire 3D volumetric imaging data in a Cartesian coordinate system (x, y, z), conventional OCT system perform fast scanning along axial (z) dimension. By mechanically tilting the probing beam, multiple Ascans form a Bscan in x-z domain. Multiple Bscans form a Cscan in x-y-z domain. Such a raster scanning approach leads to limited spatiotemporal resolution in OCT imaging. Consider OCT data acquired from an *en-face* plane (x-y plane) at a specific depth. In order to obtain an *en-face* image, conventional OCT system has to scan the entire 3D volume and select pixels within the plane through post processing. The 3D scanning generates a vast amount of data. This 3D data cube is a huge burden for data management, including signal transferring, processing and storage. In addition, the scanning strategy using mechanical scanners like galvanometers, MEMS scanners and scanning motors further limits the imaging speed of the whole system.

This dissertation seeks to overcome limitations of conventional raster scanning approach for OCT data acquisition, by investigating novel methods to address OCT voxels in 3D space. Scanless OCT imaging is achieved through the use of spatial light modulator that precisely manipulates light wave to generate output with desired amplitude and phase. Two scanless OCT imaging technologies were investigated and validated. First, an optically computed optical coherence tomography (OC-OCT) technology was developed for volumetric imaging. OC-OCT performs Fourier transform signal processing optically before data acquisition. In addition, line field Fourier domain OCT (LF-FDOCT) based on a spatial light modulator was developed. LF-FDOCT is achieved by generating a line pattern at the SLM, projecting the SLM plane to the sample and reference arm, and performing scanning electronically by the SLM.

1.2 Dissertation Organization

This dissertation is organized as followed.

Chapter 1 describes the background and motivation of this dissertation study.

Chapter 2 discusses the principle of optical interferometry and light-tissue interaction, and provides an introduction on principle and performance of time-domain OCT (TD-OCT) and Fourier-domain OCT (FD-OCT). This chapter also presents a brief introduction on OCT applications.

Chapter 3 describes and compares OCT scanning technologies.

Chapter 4 describes the principle and experimental results of optically computed optical coherence tomography for volumetric imaging.

Chapter 5 describes the principle and experimental results of line field Fourier domain OCT based on a spatial light.

CHAPTER 2

OCT BASICS

2.1 Light Propagates As Electromagnetic Wave

Equation (2.1) shows Maxwell's Equation that describes the behavior of electric and magnetic fields.

$$\nabla \cdot E = 0$$

$$\nabla \times E = -\frac{\partial B}{\partial t}$$

$$\nabla \cdot B = 0$$

$$\nabla \times B = \mu_0 \varepsilon_0 \frac{\partial E}{\partial t} \tag{2.1}$$

In Equation (2.1), ε_0 is the permittivity of free space, and μ_0 is the permeability of free space, and E is electric field, B is magnetic field. [33][34].

Electromagnetic wave Equation in a vacuum could be obtained using Maxwell's equations (Equation (2.1)). In a vacuum and charge-free space, these equations are:

$$\frac{1}{{c_0}^2}\frac{\partial^2 E}{\partial t^2} - \nabla^2 E = 0$$

$$\frac{1}{{c_0}^2}\frac{\partial^2 B}{\partial t^2} - \nabla^2 B = 0 \tag{2.2}$$

Where $c_0$is the speed of light in free space,

$$c_0 = \frac{1}{\sqrt{\mu_0 \varepsilon_0}} = 2.99792458 \times 10^8 \; m/s$$

Maxwell's equations take the property of linearity in vacuum. Thus, electromagnetic wave Equation can be decomposed into a superposition of sinusoids. The sinusoidal solution of the electromagnetic wave Equation is shown below,

$$E(r,t) = E_0 \cos(\omega t - k \cdot r + \phi_0)$$

$$B(r,t) = B_0 \cos(\omega t - k \cdot r + \phi_0) \tag{2.3}$$

In Equation (2.3), r is the wave propagation distance, t is time (in seconds), ω is the angular frequency (in radians per second), $\omega = 2\pi f$ where f as the frequency of wave. k is the wavenumber, $k = \frac{2\pi}{\lambda}$ where λ as the wavelength. ϕ_0 is the phase angle.

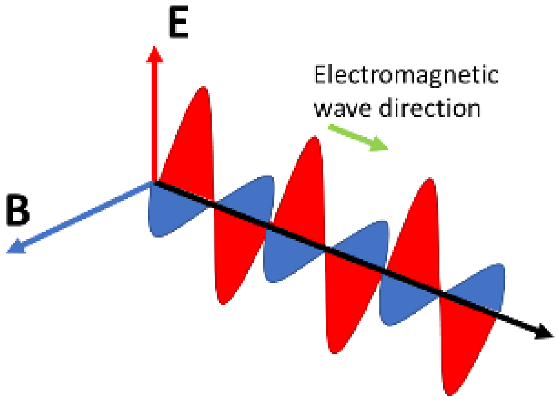

Figure 2.1 Electromagnetic wave propagation model.

As shown in Figure 2.1, E and B are perpendicular to each other and to the direction of wave propagation. The changing magnetic field creates a changing electric field through Faraday's law. The electric field creates a changing magnetic field through Maxwell's addition to Ampère's law. This perpetual cycle allows electromagnetic wave to travel through space at speed c.

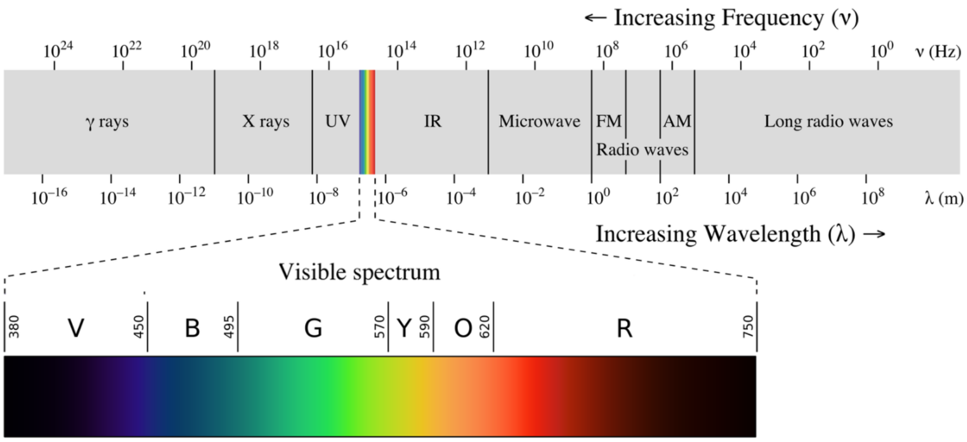

Figure 2.2 Electromagnetic Spectrum.

As shown in Figure 2.2, electromagnetic (EM) wave is classified by wavelength into radio, microwave, infrared, visible, ultraviolet, X-rays and gamma rays. The behavior of EM radiation and its interaction with matter depends on its frequency. Frequency is inversely proportional to wavelength. Electromagnetic wave at wavelength from 400 nm to 760 nm is called visible light as observable to human bare eye. Wavelength from ultraviolet to infra-red is considered as the light wave, the main research area of optics.

2.2 Light-tissue Interactions/Tissue Optics

As discussed above, light propagates as an electromagnetic wave. OCT technique utilizes near-infrared frequency light to reveal subsurface structure of biological tissue. When light interacts with matter, scattering and absorption occur. In biological tissue, optical refractive index has spatially heterogeneous distribution, which causes the light scattering. The refractive index of tissue depends on its constituent and mass density. Hence, light scattering is the result of spatial heterogeneity of optical refractive index, or spatial heterogeneity of tissue characteristics. OCT signal relies largely on the light scattering effect. Different tissues have different features under OCT imaging (i.e., lipid membrane, collagen fibers, the size of nuclei, hydration status in the tissue, etc.).

The relationship between optical refractive index and the local tissue property could be described as:

$$n = n_0 + \alpha\rho \tag{2.4}$$

where n_0 represents the refractive index of the liquid medium (i.e., water), ρ as the mass of the tissue solids over volume which could vary from 0 to 1 such as proteins, DNA, RNA, lipids, etc., α is the proportionality parameter [1].

The process of light scattering could be explained as the follows. Consider electromagnetic wave with unit magnitude and a sample with spatially heterogeneous refractive index. Light propagating in the z direction. A spherical wave $E_z(\mathbf{r})$ will be generated after light interacts with the scattering particle. The spherical wave observed at 3D coordinate **r** is:

$$E_z(\boldsymbol{r}) = \boldsymbol{g}(\boldsymbol{z}, \boldsymbol{z_0})\frac{e^{jkr}}{r} \tag{2.5}$$

where $r = |\mathbf{r}|$, $\boldsymbol{g}(\boldsymbol{z}, \boldsymbol{z_0})$ as a complex vector indicates the scattering amplitude.

As light propagates, the incident light attenuates because of scattering and absorption. The scattering cross-section is commonly used to describe the characteristics of scattering. Scattering cross-section as the geometrical cross-section, produces the same quantity of scattering power from all sides of the particle. This can be expressed as:

$$\sigma_s = \int_0^{4\pi} |\boldsymbol{g}(\boldsymbol{z}, \boldsymbol{z_0})|^2 \, d\theta \tag{2.6}$$

Another relative parameter, total cross-section (σ_t) is defined as:

$$\sigma_t = \sigma_s + \sigma_i \tag{2.7}$$

where σ_i is the absorption cross-section.

In a simplified model, the attenuation of light can be described by Beer's Law, as shown below:

$$\mathrm{A} = \mathrm{e}^{-\varepsilon \, \mathrm{l} \, \mathrm{c}} \tag{2.8}$$

where ε is the molar attenuation coefficient or absorptivity of the attenuating species, l is the optical path length and c as the concentration of the attenuation species. A more general form of the Beer's law states that, for N attenuating species in the sample,

$$\mathrm{T} = e^{-\sum_{i=1}^{N} \sigma_i \int_0^l n_i(z)dz} = 10^{-\sum_{i=1}^{N} \varepsilon_i \int_0^l c_i(z)dz} \tag{2.9}$$

where σ_i is the attenuation cross section of the attenuating species, n_i is the number density, ε_i is the molar attenuation coefficient or absorptivity, c_i is the amount concentration and l is the path length of the light beam [9]. Light absorption provides information about the sample such as chemical composition, tissue oxygenation, oxygen consumption and blood hemodynamic, etc. [2]. According the Beer's law, the penetration depth of light into the tissue is determined by absorption and scattering properties of the biological specimens. For most biological applications, near-infrared light is usually employed for OCT imaging because of small light absorption. For OCT imaging, the dominant light tissue interaction mechanism is scattering. With coherence gating, OCT eliminates photons experiencing multiple scattering events [3- 5].

2.3 Principles of Optical Coherence Tomography (OCT)

Tomography technique indicates the cross-section imaging capability from a three-dimensional object. Tomographic imaging plays a significant role in fundamental research and clinical patient management. Tomographic imaging technologies such as CT and MRI are critical in clinical diagnosis for a variety of diseases. First demonstrated in 1991, optical coherence tomography (OCT) utilizes low coherence interferometry to generate the high resolution, cross-sectional tomographic images of biological tissues [6]. Figure 2.3 shows a typical 2D OCT image. Compared to ultrasound imaging that relies on the echo of sound wave, OCT generates tomographic imaging by the echo of light, and has higher spatial resolution and faster imaging speed.

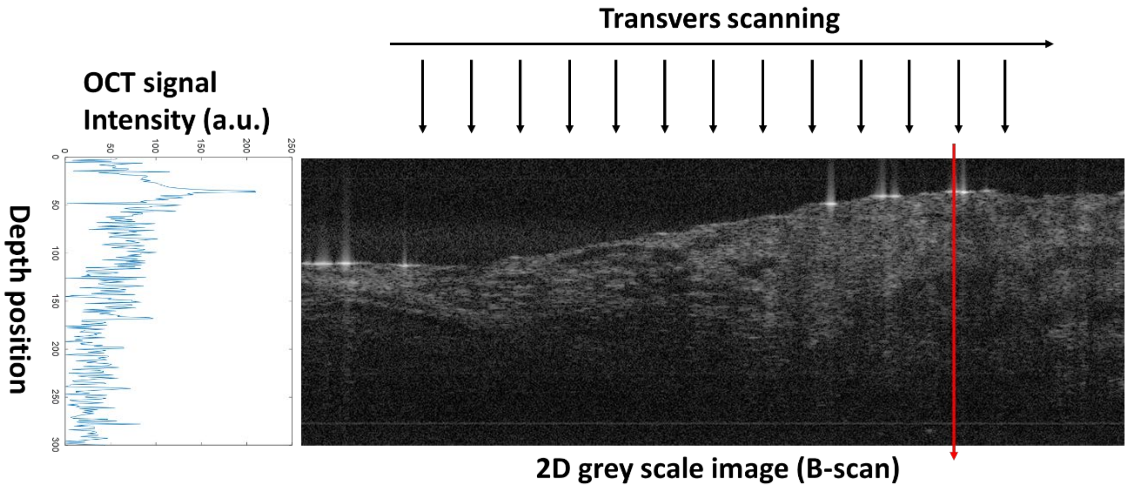

Figure 2.3 Generation of cross-sectional images by OCT through the measurement of the magnitude and echo time delay of backscattered light from the different transverse positions. The data on the left side is the Ascan data along the red line in the 2-D Bscan image on the right. The 2-D Bscan data is obtained by repeating the same process along the transvers direction. After multiple transvers scanning, the 2-D Bscan is finished. a two-dimensional data set is displayed as a grayscale or false color image.

After three decades of development, OCT has been widely used for biomedical research and clinical applications. Compared to conventional medical imaging modalities (CT, ultrasound and Magnetic Resonance Imaging), OCT has high spatial resolution (1μm

- 10μm) to reveal fine structural details of biological tissue. In addition, OCT provides extremely high scanning speed (typically faster than 100, 000 A-scans per second, or 100 B-scan frames per second) for real-time imaging.

2.3.1 Coherence and Interference.

OCT technique is established based on low coherence interferometry. In physics, two wave sources with the same frequency and waveform are said to be coherent when they have a steady phase difference. Ideally, coherent waves allow stationary (i.e, temporally and spatially constant) interference.

In OCT, interference phenomenon is used to measure the optical path length traveled into the sample by a light wave. Light travels at an extremely high speed and it is challenging if not impossible to measure the echo time of light using electrical devices. The echo time delay of the backscattered light can be measured using an interferometer. Information with high sensitivity and high dynamic range could be extracted. For OCT, low coherent light is to illuminate the interferometer.

The principle of OCT is illustrated in a Michelson interferometer is shown below.

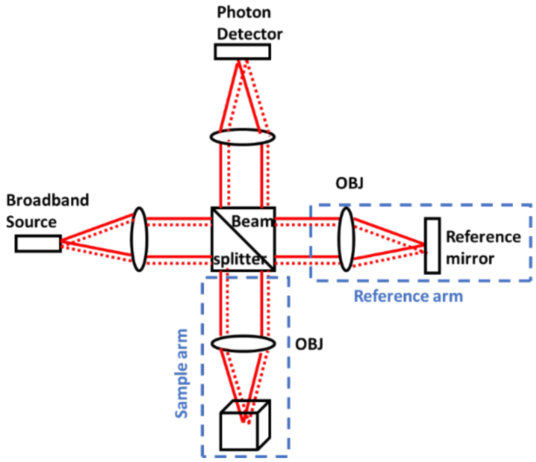

Figure 2.4 Schematic of a Michelson interferometer.

Figure 2.4 shows the schematic of the Michelson interferometer. The output of the light source is divided by a beam-splitter into two paths. One goes to the sample arm and the other goes to the reference arm. Afterwards, the optical fields reflected from the sample and the reference arms recombine and interfere. After detection, the light interferogram will be sampled, digitized and transferred to PC. In the OCT system, a broadband light source is used. As a result, interference happens only when the difference in optical path length ($\Delta l = l_s - l_r$ where l_s indicates optical path length in the sample arm and l_r indicates optical path length in the reference arm) is within coherence length. As the measure of the coherent property, coherence length (l_c) is inversely proportional to the optical source bandwidth. Built on the low coherence interferometry, the axial resolution of OCT imaging relies on the coherence length (l_c) of the broadband light source. For a coherent light source that has a large coherence length and $l >> \Delta l$, the interferometric fringe has a large magnitude and high contrast, within a large range of sample arm optical path length, as shown in Figure 2.5 (a). In comparison, for a low coherence light source that has a small coherence length, the interferometric fringe diminishes beyond a small range of sample arm optical path length, as shown in Figure 2.5 (b). In OCT, a low coherence light source provides coherence gating to resolve the depth from which signal originates.

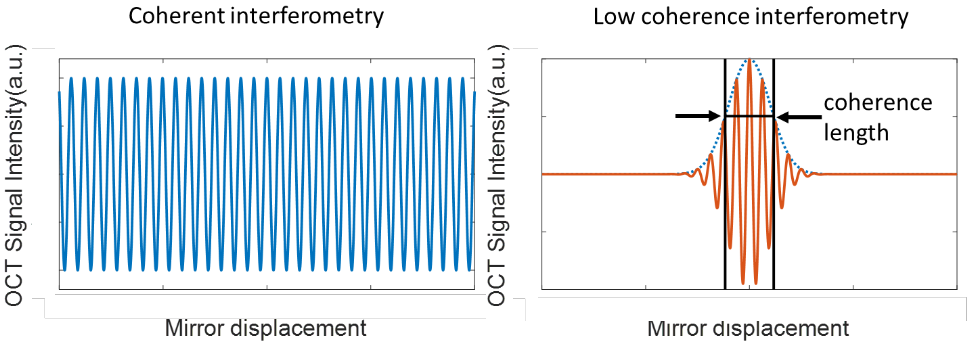

Figure 2.5 Interferometric signal with high coherence light source and low coherence light source.

2.3.2 Development of OCT technology

Optical coherence tomography based on low coherence interferometry allows depth resolved imaging. According to different measurement methods, OCT technology can be categorized into time domain OCT (TD-OCT) and Fourier domain OCT (FD-OCT).

In TD-OCT, the interference signal is obtained only when the optical path length of the sample and reference arm is matched within the narrow coherence length of the light source. The reference arm is scanned mechanically to vary the axial location from which interferometric signal originates within the sample. The recorded interference signal at different depths or relative time delays between reference and sample is then demodulated to generate a reflectivity depth profile or Ascan, as shown in Figure. 2.6 (a).

In FD-OCT systems, the interference signal is distributed and integrated over many spectral slices, and is inverse Fourier transformed to obtain the depth-dependent reflectivity profile of the sample. The main advantage of FD-OCT is that, once that a CCD based spectrometer is used, there is no need of any mechanical scanning for depth resolved imaging. All the depth information and the scattering profile are encoded in the spectral interference pattern, which is further processed easily by a personal computer. Therefore, the position of the reference arm is fixed. Hence, FD-OCT system provides a higher scanning speed compared to TD-OCT. However, in FD-OCT, the detector cost is high and complex, and the FD signal needs additional signal processing with powerful computers.

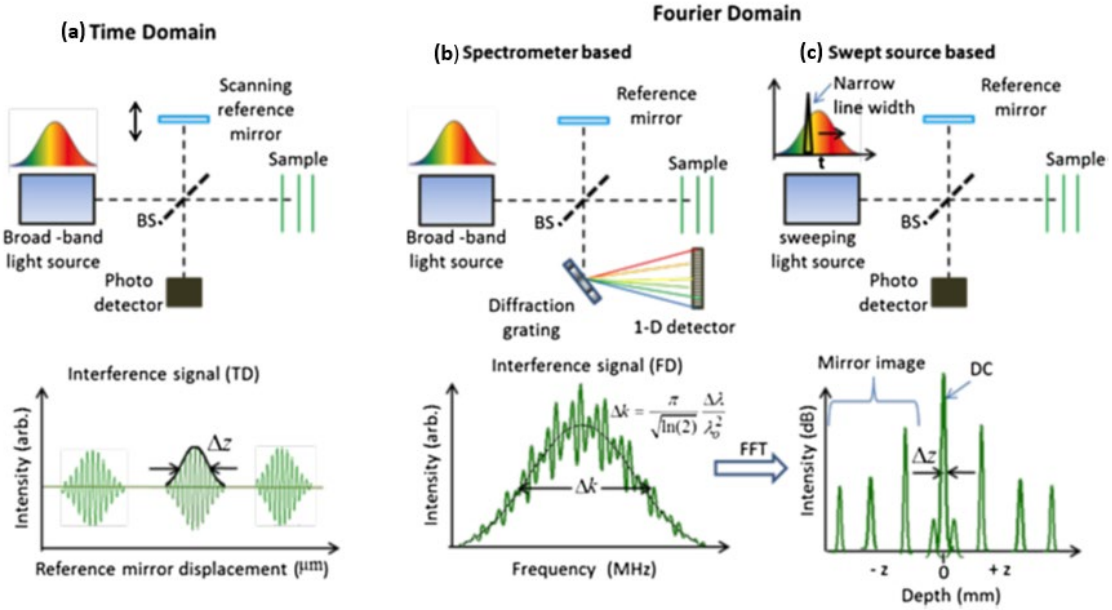

Figure 2.6 Schematic of different OCT modalities: (a) Time domain OCT (TD-OCT), two different Fourier domain OCT (FD-OCT); (b) Spectral domain OCT (SD-OCT); (c) Swept source OCT (SS-OCT).

Source: [8]

The FD-OCT could be further divided to spectral domain OCT (SD-OCT) and swept source OCT (SS-OCT) based on the different Fourier domain interferogram recording methods. Both approaches are designed based on Fourier domain interferometry. The SD-OCT approach uses a broadband near-infrared super luminescent diode (SLD) as a light source and a spectrometer to disperse light in order to transfer spatial domain light information to spectral domain. The interference signal will be dispersed by diffraction grating and further detected by a one-dimensional (1-D) array detector as shown in Figure. 2.6(b). The detected signal was sampled and digitized. Depth-resolved interferogram profile information can be obtained by performing the inverse Fourier transform.

In SS-OCT, a swept source is utilized for rapidly tuning a narrowband source within a broad optical bandwidth. Wavenumber interferogram is recorded by a single photodiode at each time stamp. Similar to SD-OCT, Fourier transform is performed to obtain depth-resolved reflectivity profile (A-scan) as shown in Figure 2.6 (c). SS-OCT does not require a scanning reference mirror or a grating for light dispersion. Moreover, by utilizing a k () wavenumber clock at the light source, the wavenumber could be linearized. SS-OCT systems has an impressively fast scanning speed, with A-scan rate ranging from 50kHz to several MHz

2.3.3 Signal characteristics and reconstruction in FD OCT

In an FD-OCT system, the optical field (E_i) output from the light source could be represented by Equation (2.10). After the beam-splitter, the output of the light source is split to sample arm and reference arm, respectively.

$$E_i = S(k, \omega) e^{(kz - \omega t)} \tag{2.10}$$

z: Sample depth

k: Wave number $k = \frac{2\pi}{\lambda} = \frac{\omega}{c}$

ω: Angular frequency

The sample can be regarded as a combination of multiple discrete layers. Hence sample profile can be expressed as the follows

$$r_s(z_s) = \sum_{n=1}^{N} r_{sn}\, \delta(z_s - z_{sn})$$

E_s and E_r can be represented as Equations (2.11) and (2.12), respectively.

$$E_s = \frac{E_i}{\sqrt{2}}\left[r_s(z_s) \bigotimes e^{i2kz_s}\right] = \frac{E_i}{\sqrt{2}}\sum_{n=1}^{N} r_{sn}e^{i2kz_{sn}} \tag{2.11}$$

$$E_r = \frac{E_i}{\sqrt{2}}\, r_r e^{i2kz_r} \tag{2.12}$$

The detected signal (I_d) is proportional to square of the combined electrical fields (Eq 2.13).

$$I_d(k,\omega) = \frac{\rho}{2}\left|E_r + E_s\right|^2$$

$$= \frac{\rho}{2}\left|\frac{S(k,\omega)}{\sqrt{2}}\, r_r e^{i(2kz_r-\omega t)} + \frac{S(k,\omega)}{\sqrt{2}}\sum_{n=1}^{N} r_{sn}e^{i(2kz_{sn}-\omega t)}\right|^2 \tag{2.13}$$

As the bandwidth of commercial electronic devices generally cannot measure fast temporal fluctuation of the optical fields, ensemble average of Equation (2.13) is performed in measurement and terms with ω can be simply eliminated. Equation (2.13) becomes:

$$I_d = \frac{\rho}{4}\left[S(k)(R_R + R_{s1} + R_{s2} + R_{s3} + \cdots)\right]$$

$$+ \frac{\rho}{4}\left[S(k)\sum_{n=1}^{N}\sqrt{R_{sn}R_R}\left(e^{i2k(z_r-z_{sn})} + e^{-i2k(z_r-z_{sn})}\right)\right]$$

$$+ \frac{\rho}{4}\left[S(k)\sum_{n\neq m=1}^{N}\sqrt{R_{sn}R_{sm}}\left(e^{i2k(z_{sn}-z_{sm})} + e^{-i2k(z_{sn}-z_{sm})}\right)\right] \quad (2.14).$$

According to Equation (2.14), OCT signal has three parts: DC term, cross-correlation term and auto-correlation term. The cross-correlation term is the desired OCT interference signal.

Given Equation (2.15), I_d could be transformed from k (wavenumber domain) to z (spatial domain) using Fourier transform, as shown in Equation (2.16).

$$\cos(kz_0) \xleftrightarrow{Fourier\ transform} \frac{1}{2}\left[\delta(z+z_0)+\delta(z-z_0)\right] \tag{2.15}$$

$$\begin{aligned} I_d = {} & \frac{\rho}{8}\left[\gamma(k)(R_R + R_{s1} + R_{s2} + R_{s3} + \cdots)\right] \\ & + \frac{\rho}{4}\left[\sum_{n=1}^{N}\sqrt{R_{sn}R_R}\left[\gamma\big(2(z_r - z_{sn})\big)\right] + \gamma(-2(z_r - z_{sn}))\right] \\ & + \frac{\rho}{4}\left[\sum_{n\neq m=1}^{N}\sqrt{R_{sn}R_{sm}}\left[\gamma\big(2(z_r - z_{sn})\big)\right] + \gamma(-2(z_r - z_{sn}))\right] \end{aligned} \tag{2.16}$$

2.3.4 Performance of OCT system

(a) Spatial resolution

In OCT imaging, axial resolution and lateral resolution are decoupled. The axial resolution in OCT is determined by the center wavelength and bandwidth of the light source. The coherence length is proportional to the width of the field autocorrelation measured by the interferometer, and the envelope of the field autocorrelation is related to the Fourier transform of the power spectrum. For a light source with a Gaussian-shaped spectrum, the axial resolution (Δz) can be defined as:

$$\Delta z = \frac{2\ln(2)}{\pi}\frac{\lambda_0^2}{\Delta\lambda} \tag{2.17}$$

where Δz is the full-widths-at-half-maximum (FWHM) of the autocorrelation function, λ_0 is the central wavelength and $\Delta\lambda$ is the bandwidth of the light source, respectively.

Central wavelength and bandwidth of light source could also affect penetration depth of the sample tissue, as longer wavelength light has better penetration capability. As shown in Equation (2.17), axial resolution is inversely proportional to the bandwidth of the light source.

On the other hand, transverse or lateral resolution in OCT imaging is determined by the diffraction-limited spot size of the focused optical beam. The diffraction-limited minimum spot size is inversely proportional to the numerical aperture (NA) or the focusing angle of the beam. The transverse resolution (Δx) is given as:

$$\Delta x = \frac{4\lambda_0}{\pi} * NA \tag{2.18}$$

In Equation (2.18), λ_0 is the central wavelength, NA (numerical aperture) is defined as d/f where d is the diameter of the objective lens and f is the focal length of the lens. A higher lateral resolution can be achieved by using a stronger lens to focus the beam to a smaller spot. Typically, OCT imaging uses a small NA lens to achieve a better depth of focus. The lateral field of-view for a point-by-point scanning OCT system is determined by the deflecting angle of the beam which is proportional to the voltage applied to the galvanometer for beam scanning and the focal length of the imaging objective.

(b) Sensitivity of OCT:

In OCT, weak sample light interferes with a strong reference light. The interference signal effectively magnifies the weak reflection from the sample arm to achieve a high sensitivity. Define $R_{s,min}$ as the weakest sample reflectivity detectable in OCT imaging. $R_{s,min}$ generates a signal level equal to the noise level of the OCT system. The sensitivity (S) is defined as the ratio of the signal power generated by a perfectly reflecting mirror ($R = 1$) and that generated by $R_{s,min}$:

$$S = \left.\frac{1}{R_{s,min}}\right|_{SNR=1} \qquad (2.19)$$

There are three main noise sources in OCT: shot noise, excess intensity noise and receiver noise. With a sufficiently large reference power, shot noise dominants. With shot noise limited detection, the sensitivity can be expressed as:

$$S = \frac{\alpha}{4}\frac{P_s}{q_e B} \qquad (2.20)$$

In Equation (2.20), $\alpha = \frac{q_e\eta}{h\nu}$, q_e is the electron charge, η is the quantum efficiency, $h\nu$ is the photon energy, P_s is the source power and B is the bandwidth of the light source. As shown in Equation (2.20), sensitivity in OCT imaging is proportional to the source power and is inversely proportional to the electronics bandwidth. In a typical OCT system, when source power is low, receiver noise limits the sensitivity of the system. However, at higher power source situation, the existence of excess noise does not determine the senstivity.

2.3.5 OCT data representation

OCT data can be gathered and displayed in a few different formats (A-scan, B-scan and C-scan).

(a) Ascan OCT image:

Ascan OCT image demonstrates the one-dimensional reflectivity or depth-resolved profile at a specific transverse coordinate. Figure 2.7(a) shows a typical Ascan image. It represents the intensity of the backscattered signal from the sample at different depth in axial direction.

(b) Bscan OCT image:

Bscan OCT image provides the cross-sectional image from the sample. A two-dimensional graphical image is presented. It is obtained by performing Ascan acquisition at different transverse coordinates. Figure 2.7 (b) shows the B-scan or cross-sectional of retinal image.

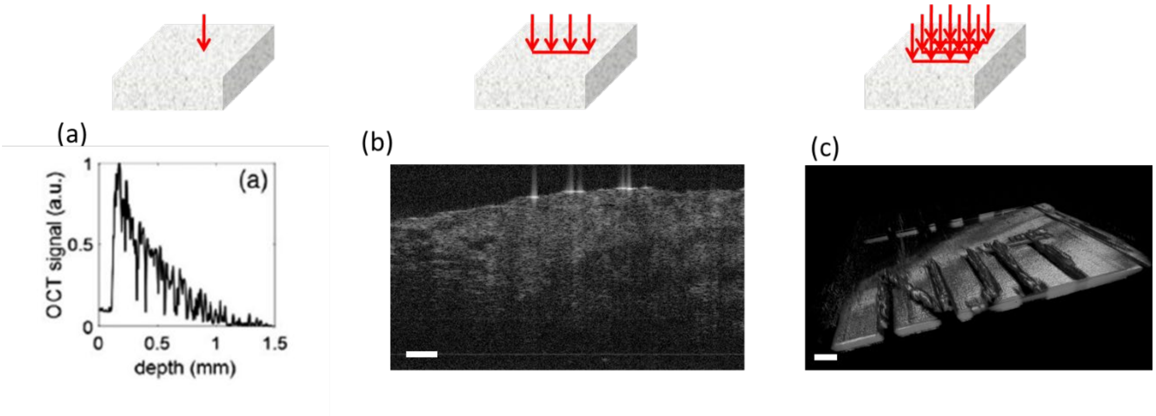

Figure 2.7 Three OCT imaging display modalities: (a) A-scan, depth resolved 1-D data by scanning a single point (b) B-scan or cross-sectional image, 2-D image by assemble multiple a scans (c) C-scan image. Here,3-D volumetric image using multiple B-scans, 3D phantom with the "NJIT" pattern is used as sample to acquire the images. White bar indicates 200 µm.

Source:[6]

(c) Cscan OCT image:

Cscan image (3D) is obtained by performing Bscan at different elevation coordinates. 3D rendered volumetric data is generated using a series of Bscan images. Figure 2.7(c) shows a 3D volume cubic of an NJIT sample. We can clearly see the letters with clear edges.

2.4 OCT Applications

2.4.1 Ophthalmology

OCT was demonstrated in retinal imaging in ophthalmology, and has made significant clinical contributions to ophthalmology [10]. Retina is optically accessible, and has multiple layers with different thicknesses and light reflectivity. As a result, one of the most successful application of OCT is in retinal imaging. After *in vivo* retinal images were obtained first in 1993 [11,12], ultrabroad-bandwidth light sources have been employed to obtain ultrahigh-resolution (UHR) OCT techniques. New ultrabroad bandwidth light sources have enabled a significant advance in OCT resolution (Fig. 2.8). OCT technique for the first time enabled a direct photo detector loss correlation with retinal function in Stargardt's dystrophy using UHR source [15]. With the UHR source, OCT is further utilized for therapy monitoring and disease pathogenesis [16–18].

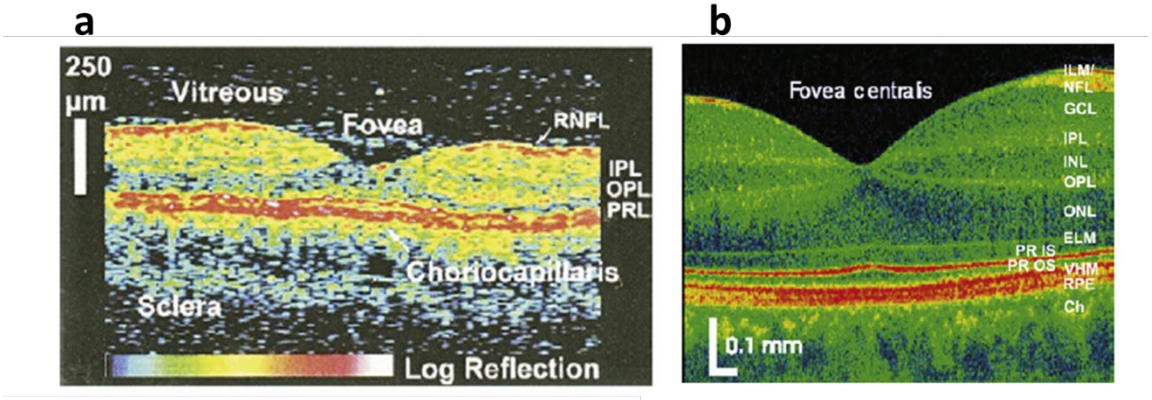

Figure 2.8 Resolution in ophthalmologic OCT: (a) A-scan TD-OCT. SLD: λ=843nm, $\Delta\lambda$=30nm, lc=10μm. 100 A-scans were obtained within 2.5 seconds, (b) FD-OCT. Ti-Sapphire-Laser: λ=800nm, $\Delta\lambda$=260nm, lc=1μm. And with dispersion numerically corrected.

Source: [13]. [14];

As TD OCT evolved to high-sensitivity FD detection techniques, high-speed and 3D OCT imaging became possible. Advanced source allowed OCT to achieve a larger penetration depth to image the choroid of retinal. Transverse resolution of OCT is further improved by adaptive optics. Additionally, functional OCT techniques have been developed such as Doppler-OCT, spectroscopic OCT and polarization-sensitive OCT for new applications.

2.4.2 Cardiology

Cardiology is another field where OCT finds applications. The structural integrity of the vasculature in the coronary artery was scanned and examined using OCT. Functional OCT systems, such as spectroscopic OCT and PS-OCT, have been developed for cellular or molecular analysis for cardiology applications [21-26]. To further advance cardiology application of OCT for *in vivo* cardio vasculature imaging, several technological developments have been made, such as the development of rotational catheter-based probes, the improvement of acquisition speed, and the introduction of functional OCT modalities.

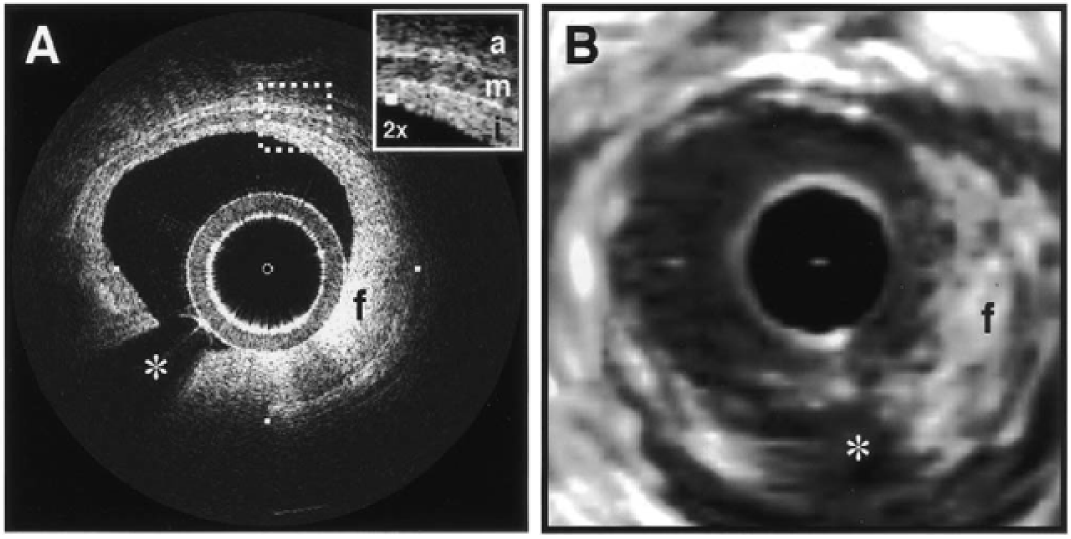

Figure 2.9 Resolution in cardiology OCT: (a) an intravascular OCT image showing a clear delineation of layers, including the internal and external elastic lamina. A fibrous plaque (f) is visible and partially obscured by a guidewire shadow artifact (*) (b) corresponding 30-MHz IVUS image at the same location.

Source: [20].

Compared to intravascular ultrasound (IVUS), OCT provides much higher special resolution as shown in Fig. 2.9 (a) and (b) [20]. In addition, probes with OCT sample-arm optics integrated into intravascular catheters have been developed, making forward and radial OCT imaging capability possible. [27,28] Catheter-based imaging could be acquired by manually feeding the probe through the vasculature or pulling it through. With high-speed data acquisition, *in vivo* real time OCT imaging can be performed for cardiology examination and guidance of interventional procedures.

2.4.3 Oncology

OCT also found applications in the field of oncology. OCT imaging has been performed on a broad spectrum of malignancies including those arising in the breast, bladder, brain, gastrointestinal, respiratory, and reproductive tracts, skin, ear, nose, and throat. The main purpose of OCT imaging in oncology is to locate the surgical margins and the early detection of small lesions. OCT imaging can help early detection and intervention of cancer.

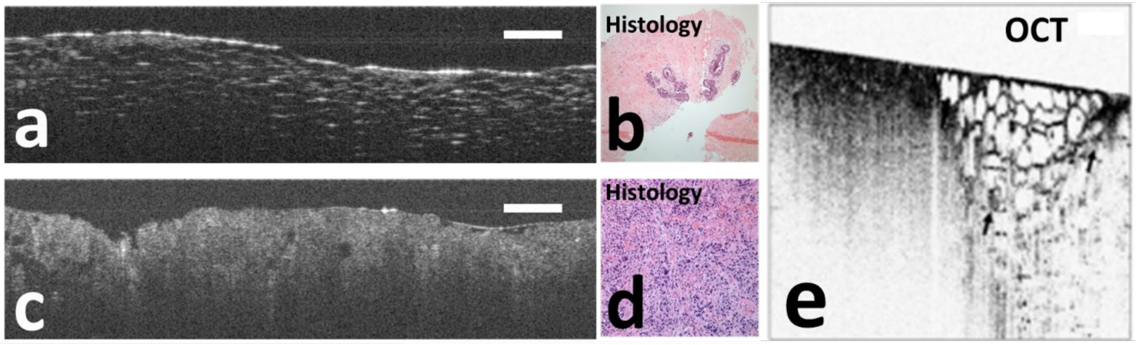

Figure 2.10 OCT image of the human breast with tumor: (e) the margin between invasive ductal carcinoma (left side) and normal fatty tissue (right side). The OCT and hematoxylin and eosin stained histological section correspond well.

Source: [29] [35].

The application of OCT in oncology was demonstrated in rat mammary tumor models [29], which proved the potential of OCT as an effective tool for the detection of lesions in the human breast. A significant structural difference was observed between normal fatty tissue and tumor tissue. The fibro-fatty tissue comprising most of the breast, and the densely scattering tumor tissue arises from within the functional epithelial network of ducts and lobules are shown in Figure. 2.10. By analyzing the spatial frequency content of the axial scattering response, highly sensitive tissue classification could be performed to distinguish normal tissue and invasive ductal carcinoma lesions [30]. Although OCT imaging could show clear difference between normal and tumor tissue, the internal location of most breast tumor remained unknown. This limits OCT application to open surgical procedures. To overcome this limitation, needle-based imaging devices are required for further development.

Another application of OCT is to assess tumor margin during surgical removal of the tumor. OCT was employed to scan freshly excised breast tissues during lumpectomy procedures. In conventional surgical procedures, to evaluate the surgical margin, the initial gross pathological evaluation of the mass is performed, which is followed by light microscopy examination of frozen or paraffin embedded tissue sections. This procedure is both time and labor consuming. It also has limited spatial sampling capability, and is affected by artifacts [31]. Using OCT to image the top 1 to 2 mm of the entire tissue surface immediately after resection, the margin status can be assessed quickly and thoroughly. This enables the surgeon to resect additional tissue immediately, if necessary [32].

CHAPTER 3

REVIEW OF OCT SCANNING TECHNOLOGIES

3.1 Point by Point Scanning

Point by point scanning in lateral dimension is the most basic scanning strategy of OCT imaging. The configuration of a typical point by point scanning OCT system is shown in Figure. 3.1.

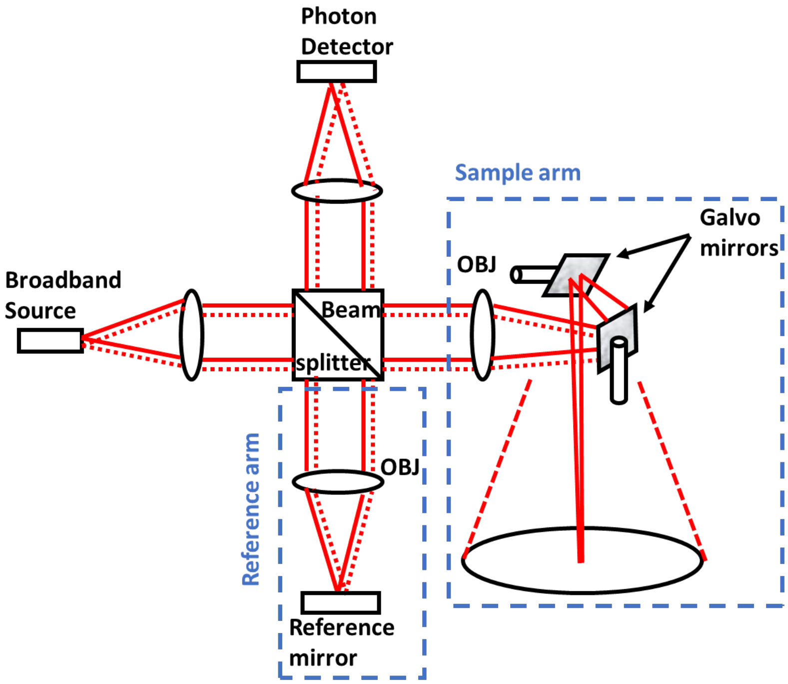

Figure 3.1 Configuration of a typical point by point scanning OCT.

In general, a near-infrared broadband light source is employed in OCT system (usually 1.3 µm or 1.06 µm central wavelength). The broad band light source illuminates an interferometer with a sample arm and a reference arm. In the sample arm, a lens is utilized to focus the probing beam and collect backscattered photons. The light reflected from reference arm and the light reflected or backscattered by the sample interfere. The interference signal is detected and transferred to a computer. By utilizing graphic processing units, parallel computation is enabled for real time signal processing and image display. For Fourier domain imaging, an A-scan along z direction (axial direction) is obtained with the beam located at a specific lateral coordinate. Volumetric OCT data is acquired by scanning the beam two-dimensionally with a pair of galvanometers. A galvanometer is an electromechanical instrument that produces a mechanical rotation after sensing an electric current. By attaching the mirror with the galvanometer, a mirror galvanometer is assembled. With a specific electric voltage input to mirror galvanometer, a corresponding deflection angle of mirror can be achieved to steer the light beam to the desired destination. The galvanometer is synchronized with the camera to perform lateral scanning. Multiple cross-sectional images could be obtained from a three-dimensional (3D) data set. On the other hand, with volumetric OCT data obtained, the 3D data volume can be reduced to a 2D image by taking a single slice or averaging multiple layers in post processing.

3.2 Line Scanned OCT

Line field OCT (LF-OCT) takes a different approach for lateral scanning. Line field OCT can be implemented using a cylindrical lens as illustrated in Figure 3.2 With the cylindrical lens, a line field was generated on the sample and reference mirror.

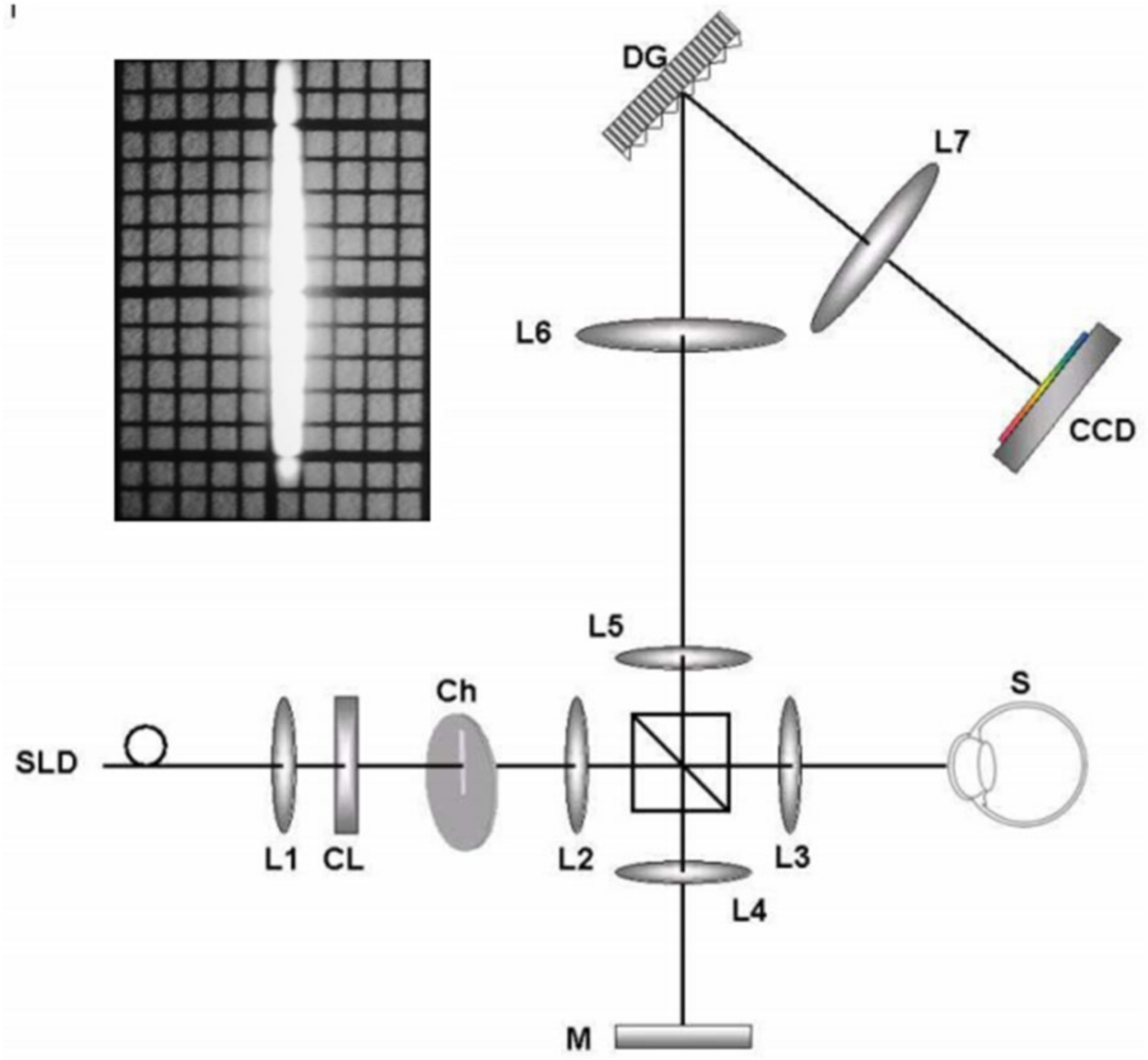

Figure 3.2 Configuration of line field OCT. SLD as the super luminescent diode. L1 L2 L3 L4 L5 L6 L7 as objective lenses. CL as the cylindrical lens. Ch as the chopper wheel. DG as the diffraction grating. CCD as the camera. It generates a slit illumination by using the collimated light passing through a cylindrical lens with A chopper wheel placed at its focal plane. With the cylindrical lens, a line field was generated on the sample and reference mirror. The line illumination can be viewed as a set of parallel channels, each of them associated with a different lateral position on the sample. These channels are spectrally dispersed by the diffraction grating and recorded individually on different rows of the CCD area.

Source: [62].

The combined signal from the sample arm and reference arm is dispersed by a grating and detected by a 2D camera. Each row of the 2D camera detects an interferometric spectrum from a corresponding lateral coordinate. By performing Fourier transform along the rows, a Bscan image is obtained. Although LF-OCT cannot provide a 3D volume data directly, LF-OCT is sufficient to provide reliable 2D B-Scan of layer thickness measurement values. Line scanned OCT enabled OCT B-Scan image in a single shot. The SNR and sensitivity of the Fourier domain LF-OCT were reported to be higher than the time domain FF-OCT.

3.3 Full Field OCT

Another OCT scanning technologies is full field optical low-coherence (FF-OCT). As an effective way to produce micrometer-resolution cross-sectional images from biological tissues, OCT generates 2D and 3D images at a limited lateral resolution (10-30 μm) by using a mechanical scanning device. In the sample arm, the beam is not tightly focused, so that the confocal length is greater than the imaging depth. Full field OCT is another parallel OCT imaging technique that achieves high lateral resolution, as illustrated in Figure 3.3.

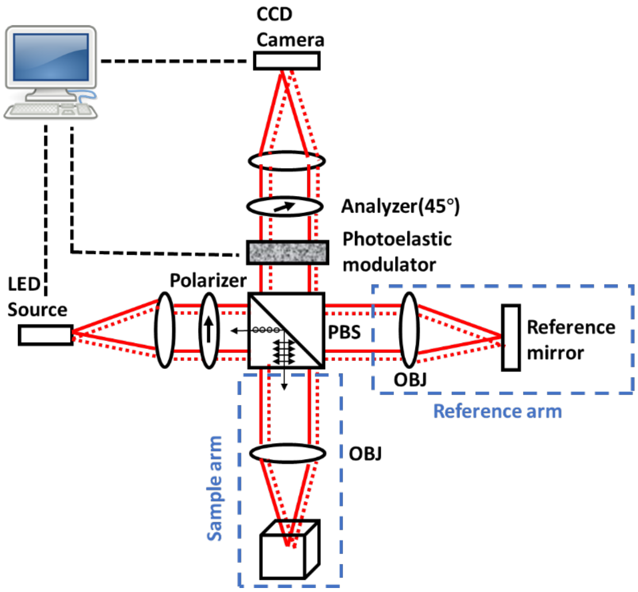

Figure 3.3 Configuration of a typical Full Field OCT.

A beam splitter separates the beam into sample arm and reference arm. The reflected signal is recombined. The recombined beam is elliptically polarized. Its polarization state is measured to provide the value of the orthogonal components. This measurement is achieved by using lock-in detection technique with a photo elastic polarization modulator associated with an analyzer [46-48]. As the CCD maximum readout frequency is much lower than the modulation frequency. A synchronization relationship must be built between light source, photo elastic polarization modulator and CCD camera.

Photo elastic polarization modulator introduces a periodic phase shift between two orthogonal light, while analyzer axes remain at 45° from these two [49]. Only the interferential part could be modulated. The modulation amplitude is set approximately 2.0 rad (according to the first maximum of the Struve function H_0) [47]. The photo elastic polarization modulator is set to be the main clock for the whole system [49]. Synchronized with the photo elastic polarization modulator, the light source is set to tuning a periodic phase shift (0°, 90°, 180°, 270°). This phase is shifted at each camera readout. For each phase shift, an image is transferred to CCD camera. Four images are thus recorded for one period, corresponds to 4 phase shifts. Linear combinations of these data is proportional to the amplitude of a sinusoidal coherent backscattered component. Thus, the two-dimensional image of the sample located only in the focus plane is produced at the same time stamp.

3.4 Comparison Between Three Scanning Technique

All the above described techniques can be used to perform 3D imaging with microscopic resolution. Point by point scanning and LF-OCT takes advantage of spectrum domain interferogram processing method to generate the whole axial image without any scanning involved. However, they require a long scanning time to generate 2D images that are not in Bscan planes. The FF-OCT performs fast scanning in *en face* plane. Still, the cross talk from backscattered light is the main problem that limited the sensitivity of FF-OCT system.

CHAPTER 4

OPTICALLY COMPUTED OPTICAL COHERENCE TOMOGRAPHY FOR VOLUMETRIC IMAGING

4.1 Introduction

Optical coherence tomography (OCT) has the capability of high-resolution cross-sectional imaging. A wide range of biomedical applications of OCT has been found, in ophthalmology, cardiology and oncology [6]. High-speed OCT has been used to perform functional imaging, such as quantitative blood flow imaging, dynamic optical coherence elastography, and large-scale neural recording [36-38]. In many application of OCT, high-speed imaging in *en-face* plane is more desirable that the capability to image the entire 3D volume at a low speed. However, conventional OCT imaging system lacks the spatiotemporal resolution and flexibility to perform high speed imaging within an arbitrary 2D plane, although the acquisition of one OCT pixel on average takes an extremely short period of time [39]. Time domain (TD) OCT performs axial scanning mechanically. Ascan in TD OCT is acquired pixel by pixel in sequence. As a result, TD OCT is inherently slow. For Fourier domain OCT (FD OCT), an entire Ascan scan is generated by capturing a spectral domain interferogram and performing Fourier transform on the interferogram. Comparing to TD OCT, FD OCT is able to generate all the pixels within an A-scan without mechanical scanning. Hence the imaging speed and sensitivity are increased enormously in FD OCT compared to TD OCT [40, 41]. Nevertheless, as to the 3D volumetric data acquisition, both systems has the same challenge.

In order to acquire OCT data in a 3D Cartesian coordinate system (x, y, z), conventional TD and FD OCT system perform fast axial (z) scanning and it takes a short period of time δt to acquire a pixel in an Ascan. By mechanically scanning the probing beam, multiple Ascans form a Bscan in x-z domain. Hence it takes a time interval of N^2δt to acquire a B-scan with N^2 pixels, assuming each Ascan has N pixels and each Bscan has N Ascans. Multiple Bscans form a Cscan data cube and it takes a time interval of N^3δt to acquire a Cscan with N^3 voxels. Consider an *en face* plane (x-y plane at a specific depth) that with N^2 pixels. Given the sequential data acquisition strategy, the OCT system has to scan the entire 3D volume and select pixels within the plane through post processing. Hence, it takes a time interval of N^3δt to acquire an *en face* image that has N^2 pixels, suggesting it on average takes a time period of Nδt to acquire a pixel in the *en face* image. In addition, the 3D scanning generates a massive amount of data. It is a burden for the computer to transfer, store, and process 3D data cubes obtained. In addition to challenges in managing massive volumetric data, current scanning strategy uses mechanical scanners (galvanometers, MEMS scanners and scanning motors) and these mechanical devices further limit the imaging speed. In this study, we took an optical computation strategy to overcome the limit in current scanning method. Optical computation has been utilized in imaging studies. X. Zhang generated optical computed OCT imaging through fast temporal modulation by using arbitrary waveform generation [42]. In a different study, optical computing was used to deliver a solution to acquire massive 3D data by using photons to perform computation tasks [43].

Optically computed OCT (OC-OCT) technology developed in this study eliminates the need for mechanical scanning in 3D OCT imaging by employing a highly novel optical computation system to perform Fourier transform. For conventional Fourier domain OCT, data is acquired and transferred to PC where Fourier transform is performed to reconstruct depth profiles of the sample. OC-OCT performs signal processing optically before the signal is detected by the camera. The optical computation procedure is achieved by using a spatial light modulator (SLM). SLM is used in applications such as optical pulse shaping, structured illumination and optical computation [44, 45]. Using SLM, light wave can be precisely modulated to have the anticipated amplitude and phase. The spectral interferogram output from a spectral domain OCT system is modulated by a programmable SLM to achieve Fourier transform optically. The signal is later detected without spectral discrimination. An optically computed two-dimensional image at a specific depth determined by the SLM pattern is thus produced. The optical computation strategy allows volumetric OCT imaging without axial or lateral mechanical scanning, which is unique has not been demonstrated before

4.2 Principle of OC-OCT Imaging

OC-OCT is a Fourier domain technique that achieves depth resolution by performing Fourier transform optically. Consider an A-scan **S** ($\mathbf{S}\in\mathbb{C}^N$ and $\mathbf{S}= [s_1, s_2, s_3, \ldots, s_N]^T$). With sample light originating from a specific transverse coordinate, the interferometer generates a spectral interferogram **M** after a disperser. **M** is a 1D vector ($\mathbf{M}\in\mathbb{R}^N$ and $\mathbf{M}=[m_1, m_2, m_3, \ldots, m_N]^T$) and is mathematically related to the spatial domain A-scan through Fourier transform: $\mathbf{S}=\mathbf{FM}$ which is more explicitly shown in Equation (4.1) (s_n represents spatial domain OCT signal at the n^th^ discrete depth in an A-scan; m_k represents spectral signal at the k^th^ wavenumber; $\mathbf{F}\in\mathbb{C}^{N\times N}$ is the Fourier transform matrix and $F_{nk}=e^{j2\pi nk/N}$).

$$\begin{bmatrix} s_1 \\ s_2 \\ \cdots \\ s_N \end{bmatrix} = \begin{bmatrix} F_{11} & F_{12} & \cdots & F_{1N} \\ F_{21} & F_{22} & \cdots & F_{2N} \\ \cdots & \cdots & \cdots & \cdots \\ F_{N1} & F_{N2} & \cdots & F_{NN} \end{bmatrix} \begin{bmatrix} m_1 \\ m_2 \\ \cdots \\ m_N \end{bmatrix} \tag{4.1}$$

As illustrated in Figure 4.1 (a), a conventional FD OCT system measures the entire interferometric spectrum **M** that has N discrete Fourier bins, streams the data into a computer, performs Fourier transform in the computer and reconstructs the entire A-scan. Figure 4.1 (a) also implies N Fourier bins have to be acquired to fully reconstruct the A-scan **S**, even if a small subset of pixels are of interest in the A-scan. OC-OCT takes a completely different approach to resolve a pixel in 3D space.

According to Equation (4.1), s_n, the OCT signal at the nth discrete depth in an A-scan, can be expressed in Equation (4.2) that shows s_n is the inner product between vector $\mathbf{f}_n$ (the transpose of nth row of the Fourier matrix **F**) and vector **M**. In Equation (4.2), • indicates vector inner product.

$$\begin{aligned} s_n &= F_{n1}m_1 + F_{n2}m_2 + \cdots + F_{nN}m_N \\ &= \begin{bmatrix} F_{n1} & F_{n2} & \cdots & F_{nN} \end{bmatrix} \begin{bmatrix} m_1 \\ m_2 \\ \cdots \\ m_N \end{bmatrix} \\ &= \boldsymbol{f}_n \bullet \boldsymbol{M} \end{aligned} \tag{4.2}$$

Equation (4.2) provides an alternative approach to address a spatial location in OCT imaging. As illustrated in Figure 4.1 (b), the OC-OCT system calculates $\mathbf{f}_n \bullet \mathbf{M}$ optically and directly obtains s_n

at the point of data acquisition. Optical computation of Equation (4.2) is further illustrated in Figure 4.1 (c). The chosen Fourier basis function ($\mathbf{f}_n$) is projected to the SLM along the dimension of spectral dispersion. The spectrum modulated by the SLM is essentially the element-wise product of $\mathbf{f}_n$ and **M** ($\mathbf{f}_n \circ \mathbf{M}$). The detector then performs spectrally non-discriminative detection, generating s_n, the inner product between vector $\mathbf{f}_n$ and vector **M**.

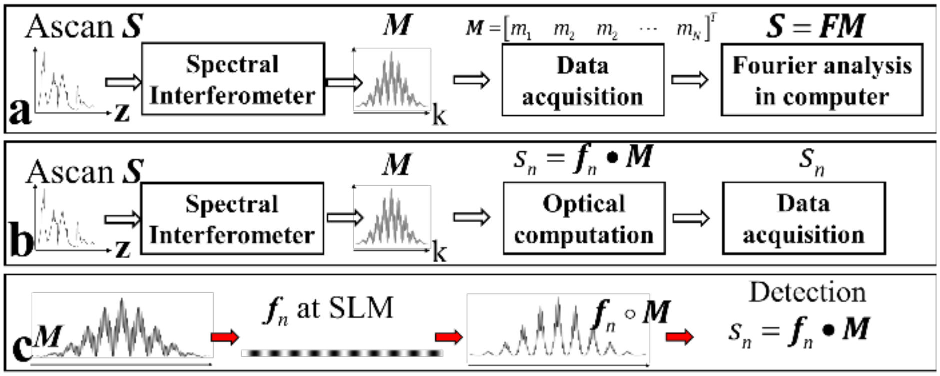

Figure 4.1. Data flow in (a) conventional FD OCT and (b) in OC-OCT; (c) Fourier transform of spectral interferogram.

The configuration of OC-OCT system that allows depth resolved imaging with an extended field of view is illustrated in Figure 4.2. The OC-OCT system uses a broadband source to illuminate the Michaelson interferometer with an extended field of view. A 2D reflective SLM is used for light modulation and a 2D camera is used for signal detection.

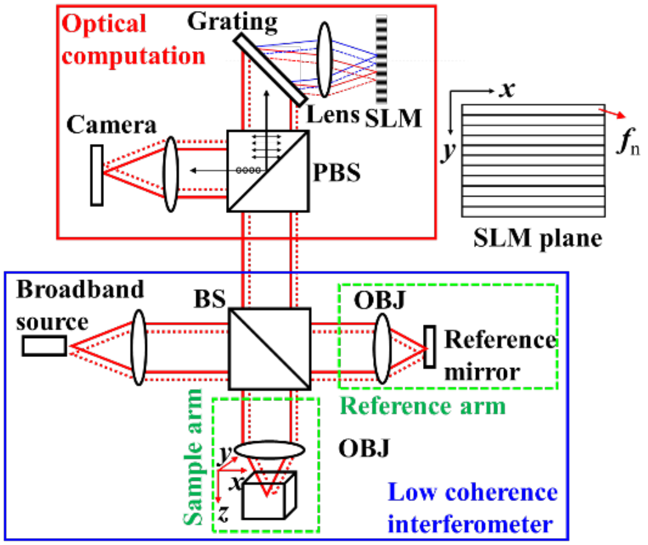

Figure.4.2. Configuration of the OC OCT system for 3D imaging. BS: beam splitter; PBS: polarization beam splitter; OBJ: objective.

The imaging principle of OC-OCT is explained as the follows. First, the OC-OCT configuration in Figure 4.2 establishes a one-to-one mapping between the transverse spatial coordinate at the sample plane and at the detector plane, illustrated as solid and dashed light beam profiles in Figure 4.2. This is similar to conventional light microscopy. Optical signal originating from transverse coordinate (x_0, y_0) at the sample is mapped to the same y coordinate $(y=y_0)$ at the detector, because the light beam is not altered along y dimension by the grating or the SLM. On the other hand, the spectrum originating from different x coordinate arrives at the SLM plane with a global shift proportional to the x coordinate after the diffraction grating. Reflected by the SLM and diffracted again by the grating, the light rays originating from (x_0,y_0) at the sample are collimated and eventually focused to (x_0,y_0) at the detector plane for spectrally non-discriminative detection, for a magnification of 1 from the sample plane to detector plane without loss of generality. On the other hand, depth resolution is achieved through optical computation. The diffraction grating disperses the output of the interferometer along x direction and the SLM projects a Fourier basis function $(\mathbf{f}_n)$ to its row at a specific y coordinate $(y=y_0)$, as illustrated in the upper right inset of Figure 4.2. Spectral interferogram originating from different x coordinate at the sample is modulated by a laterally (in x dimension) shifted version of $\mathbf{f}_n$, which does not affect the results of optical computation of OCT signal magnitude. Spectrally non-discriminative detection of the modulated interferometric spectrum generates depth resolved OCT signal from the n^{th} discrete depth, for pixels corresponding to different x coordinates. Notability, when all the rows of the SLM projects the same pattern for spectral modulation, the OC-OCT system generates an en face imaging from a specific depth. If different rows of the SLM project different Fourier basis functions, signals can be simultaneously obtained from different depths. Therefore, OC-OCT allows snap-shot imaging from an oblique plane.

OC-OCT system set up is shown in Figure 4.2. A mounted LED (Thorlabs) at 470nm with 25nm bandwidth is employed (1mm by 1mm emitter size) as the broadband source. The interferometric spectrum was dispersed by a 600/mm grating, modulated by a 2D SLM (Holoeye LC-R 720), and detected by a CMOS camera (Basler acA2000). The achromatic doublet lens in front of the SLM had a focal length of 250mm and the achromatic doublet lens in front of the CMOS camera has a focal length of 100mm. Identical objectives (20X Olympus, dry) are used in reference and sample arms of the interferometer. The lateral field of view was approximately 0.5mm by 0.5 mm, limited by the active area of camera sensor used for imaging and the magnification from the sample to the camera. The maximum axial imaging range was estimated to be 1.2mm, limited by the digital frequency of spectral modulation imposed by the SLM. To demonstrate 3D OC-OCT imaging within a large depth range, achromatic doublet is used as imaging objectives to obtain results shown in Figure 4.6. Notably, a polarized beam splitter (PBS) was inserted between the Michaelson interferometer and the optical computation module. The PBS functions as a polarizer and an analyzer and ensures that a one to one mapping between the pixel value of the SLM and light reflectivity.

Prior to imaging experiments, K(k) the mapping between the pixel index (k) in a row of SLM and the corresponding wavenumber K is calibrated, because the pixels in a row of the SLM generally do not sample wavenumber domain spectral data uniformly. The calibration was achieved by measuring the interferometric spectrum obtained from a specular sample and enforcing linear phase [12]. Axial resolution degradation at different lateral coordinates due to the nonlinearity of K(k) is moderate because of the small FOV. R(v), the mapping between the value v projected to SLM pixels and the actual light reflectivity (R) of the SLM is also calibrated, because R(v) depends on the wavelength and polarization of the incident light, and is generally nonlinear. When v takes value of Fourier basis function (F_{nk} in Eq (1)) and is directly projected to the kth pixel in a row of SLM pixels, the spectral modulation is non-sinusoidal, leading to diminished signal amplitude and ghost high harmonic peaks after optical Fourier transformation. To ensure that precise sinusoidal modulation was imposed to the interferometric spectrum, the value of $R^{-1}(F_{nK(k)})$ is projected to the kth pixel in a row of SLM pixels. Moreover, the SLM cannot directly generate complex exponential function needed in Fourier transform (Eqs (1) and (2)). Therefore, cosine and sine patterns ($F_{cos}=(\cos(2\pi nK(k)/N)+1)/2$ and $F_{sin}=(\sin(2\pi nK(k)/N)+1)/2$) are projected to the SLM. $\mathbf{f}_{cos}$ (F_{cos} with k=1, 2, 3, …) and $\mathbf{f}_{sin}$ (F_{sin} with k=1, 2, 3, …) are temporally interlaced for spectral modulation, synchronized the data acquisition with the alternation of cos and sin patterns, acquired signals from cosine and sine channels ($s_{cos}=\mathbf{f}_{cos}^T\mathbf{M}-s_{DC}$ and $s_{sin}=\mathbf{f}_{sin}^T\mathbf{M}-s_{DC}$) and extracted the magnitude of the OC-OCT signal: $I=(s_{cos}^2+s_{sin}^2)^{1/2}$. With reference light much stronger than sample light, s_{DC} could be estimated by $\sum m_k$ obtained with sample arm blocked. To simplify subsequent description, the function projected to the SLM is referred as $\mathbf{f}_n$ that was generated after wavenumber calibration, reflectivity calibration, and temporal interlacing.

4.3 Results

The z sectioning capability of OC-OCT was first validated experimentally. The axial point spread function (PSF) of the OC-OCT imaging system is assessed, using A-scans obtained from a mirror with an impulse reflectivity profile. A series of complex exponential functions ($\boldsymbol{f}_n$, n=1, 2, 3, …) is projected to different rows (different y coordinate) of SLM pixels. As a result, different rows of the detector received signals modulated by different complex exponential functions and came from different depths of the sample. The axial PSF (a 1D vector) was then obtained by averaging the image directly obtained from the camera along x direction. The axial position of the mirror is varied using a translation stage and obtained axial PSFs as shown in Figure 4.3 (a). The horizontal axis at the bottom of Figure 4.3 is the row index (n_R) of the sensor array and is linearly related to the depth z: $z = an_R+b$. The peak pixel index is correlated with the actual axial position of the sample (Figure 4.3 (b)) and extracted the values for a and b through linear fitting ($a \approx 0.17$µm and $b \approx 36.91$µm) that allowed us to convert n_R to actual depth shown as the horizontal axis at the top of Figure 4.3 (a). To evaluate the axial resolution, a Gaussian envelope is used to fit the PSFs obtained at different depths and the axial resolution of our OC-OCT system was estimated to be 5µm according to the full width half maximum (FWHM) of the Gaussian function. The theoretical axial resolution is calculated using Equation (4.3)

$$\delta z = 0.44\frac{\lambda_0^2}{\Delta\lambda} \tag{4.3}$$

With the central wavelength λ_0=470nm and the bandwidth $\Delta\lambda$=25nm, the theoretical axial resolution of our OC-OCT system is expected to be 3.9 µm. The experimental axial resolution is inferior to the theoretical value, probably because of the following reasons. First, the effective spectral bandwidth used for OCT imaging is smaller than the bandwidth of the light source (Δλ). Second, the modulation projected by the SLM may be different from ideal sinusoidal modulation.

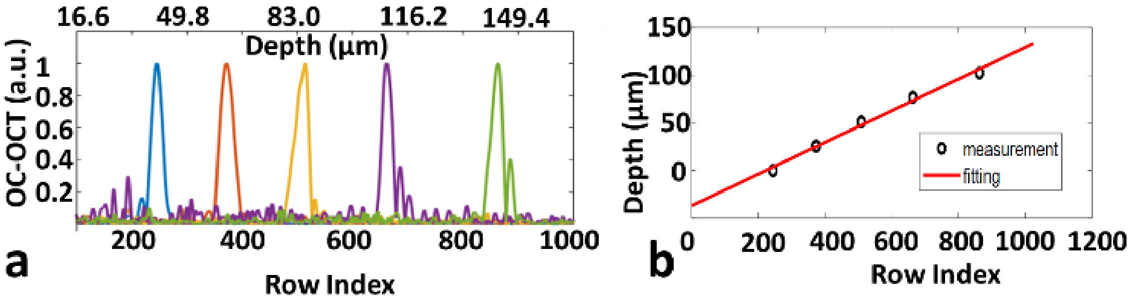

Figure 4.3. (a) A-scan obtained from a mirror at different depths; (b) linear relationship between the n_R and the actual depths.

Theoretical calculation of lateral resolution involves multiple factors. Consider a single wavelength plane wave incident into the grating (600 line per mm) and is focused to a spot at the surface of the SLM. Due to the limited spectral resolution of the grating, the size of the spot ($\delta x_{grating}$) is estimated to be 1.175μm at the sample plane using Equation (4.4). The spot size limited by light diffraction of the objective lens (δx_{obj}) is expected to be 0.72μm according to Equation (4.5), given the objective with NA=0.4 and λ_0=470nm. The lateral resolution determined by spatial sampling of the camera (δx_{camera}) satisfying Nyquist sampling theorem is estimated using Equation (4.6), given 5.5μm by 5.5μm pixels (Δx=5.5μm) of the camera and a magnification M=11 from the sample plane to the camera sensor plane. With all these factors considered, the lateral resolution δx of the OC-OCT system is estimated using Equation (4.7) and the value is 2 μm.

$$\delta x_{grating} = \frac{\lambda_0 F_{obj}}{D_{grating}} \tag{4.4}$$

$$\delta x_{obj} = \frac{0.61\lambda_0}{NA} \tag{4.5}$$

$$\delta x_{camera} = \frac{2\Delta x}{M} \tag{4.6}$$

$$\delta x = \sqrt{\left(\delta x_{grating}\right)^2 + \left(\delta x_{obj}\right)^2 + (\delta x_{camera})^2} \tag{4.7}$$

The capability of OC-OCT for depth resolved en face imaging has been demonstrated to achieve *en face* slicing of the sample at depth z0. The same modulation pattern (fn0) is projected to different rows of the SLM. The sample, a USAF1951 resolution target, is brought to depth z_0 (z_0=32.30 µm) and obtained the image shown in Figure 4.4 (a). The area within the red square is enlarged in Figure 4.4 (b), in which the smallest discernable structure is the 6th element of the 8th group, suggesting a lateral resolution of 2.2µm, similar to theoretical estimation of 2µm that considers the convolution of multiple factors (camera sampling, diffraction limit of the imaging objective, spectral resolution of the grating). The experimental lateral resolution is slightly inferior to the theoretical value, probably because of misalignment of the optical components within the imaging system.

To validate the image in Figure 4.4 (a) was indeed sectioned through optical computation, $\boldsymbol{f}_{n0}$ is projected to the top rows of the SLM and projected a constant value to pixels at the bottom rows of the SLM. The sample remained at depth z_0 and other settings remained unchanged. The resultant OC-OCT image (Figure 4.4 (c)) shows large brightness at the top and appears to be completely dark at the bottom. In Figure 4.4 (d), (e) and (f), *en face* images obtained from the resolution target when the SLM modulation pattern selected different imaging depths (z_0=32.30µm, z_0+1.25µm, z_0+2.5µm) are compared. When the virtual plane determined by the SLM moved away from sample surface, the brightness of OC-OCT image decreases.

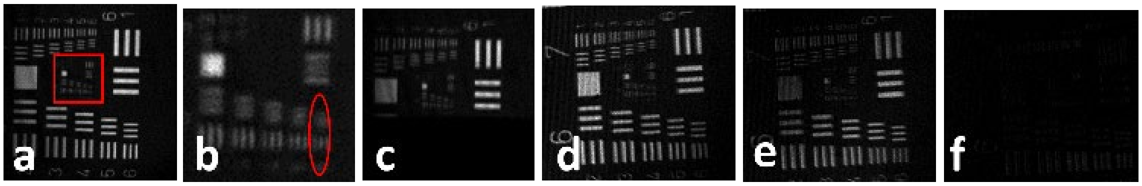

Figure 4.4. (a) *en face* image of USAF 1951 resolution target; (b) the 6th element of the 8th group in the resolution target can be resolved; (c) the top part of SLM was programed to obtain OCT signal from the resolution target; (d)-(e) *en face* images of the resolution target when the plane chosen by the SLM moved away from the sample surface.

OC-OCT for 3D imaging is validated using onion skin cells. The same Fourier basis function is projected to different rows of the SLM to obtain en face OCT image at a specific depth. By varying the Fourier basis function, en face images obtained at different depths are shown in Figure 4.5 (a), (b) and (c), with 5μm axial displacement in between. Figure 4.5 (d) is the image obtained by averaging OC-OCT signals within a depth range of 15μm.

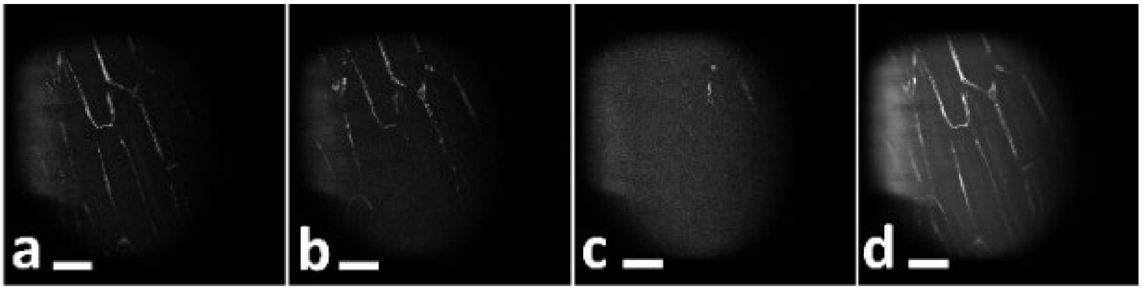

Figure 4.5. OC-OCT image of onion skin cells at different depths (a), (b) and (c); (d) image generated by averaging signal with a depth range from image a to image c. Scale bars represent 50μm.

3D rendered volume is also obtained through OC-OCT imaging. Lateral patterns are designed on a laser-plotted polyester-based photomask and a 3D phantom is fabricated by depositing photoresist layer (SU-8 2035) with 37μm elevation on silicon substrate using the photolithography facility at Brookhaven National Laboratory. The modulation function projected to the SLM is changed to acquire en face OC-OCT data from different depths for volumetric imaging. With 2D images obtained from different depth (29 en face images obtained with a 1.25μm axial interval), a 3D rendered volume is obtained (Figure 4.6 (a)). Figure 4.6 (b) and (c) show images corresponding to the surface of silicon substrate and the top of the deposited pattern. Figure 4.6 (d) is the image generated by averaging OC-OCT signal at different depths. Along the red lines in Figure 4.6 (d), cross sectional images (Figure 4.6 (e), (f) and (g)) are generated using the volumetric data. The rectangles in Figure 4.6 (e), (f) and (g) correspond to depth profiles for the areas within rectangles of Figure 4.6 (d), from which the top of the letters “I” and “T”, middle of the letter “N” and bottom of the letter “J” are discernable.

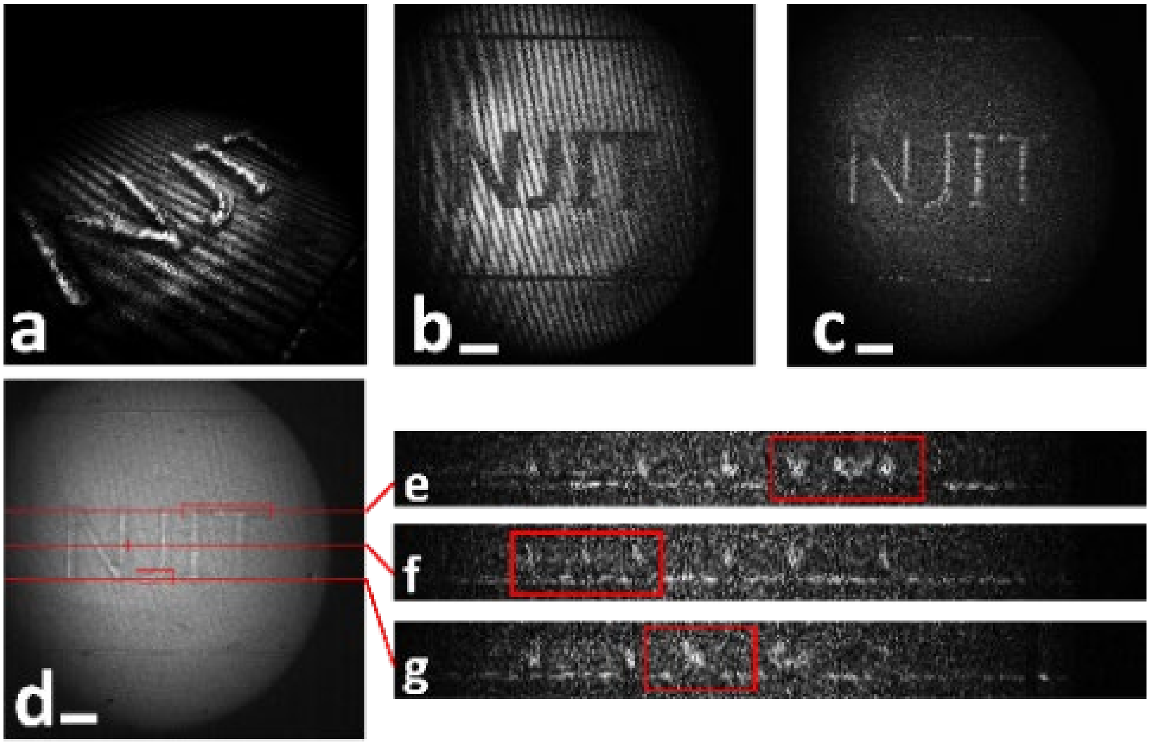

Figure 4.6. (a) 3D rendering image of 3D phantom; *en face* image from the substrate (b) and the top of photoresist layer (c); (d) *en face* image generated by averaging OC-OCT signal within a depth range of 36μm; (e)-(g) cross sectional images of three positions indicated by red lines in Figure 4.6 (d). Scale bars represent 300μm.

If fast imaging is needed in an oblique plane, the OC-OCT system can project different Fourier basis to different rows of the SLM and make the oblique plane the dimension for preferential data acquisition. For structural OCT imaging, the real and imaginary parts of complex OCT signal are measured with the SLM generating cosine and sine modulations and calculated the amplitude of OCT signal. To demonstrate complex OCT imaging, we used the cosine and sine channels output from the OC-OCT system to generate the amplitude and phase of complex signal. We projected the same modulation pattern (f_{n0}) to all the rows of the SLM to generate OC-OCT signal from depth z_0. We then used the OC-OCT system to image the substrate and the top of the 3D phantom fabricated by photolithography. The amplitude and phase images of the elevated photoresist pattern are shown in Figure 4.7 (a) and (b). The amplitude and phase images of the silicon substrate are shown in Figure 4.7 (c) and (d). In summary, the OC-OCT system described in this dissertation enabled optically computed complex OCT imaging for the first time to the best of our knowledge.

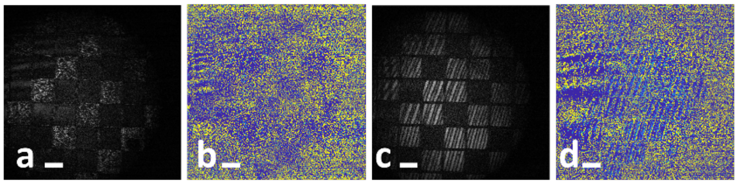

Figure 4.7, Cosine and sine channels output from the OC-OCT.

4.4 System Performance.

The imaging field of view is one of the key parameters of the system. It consists of lateral field of view and axial field of view. Because of one-to-one mapping between the sample plane and sensor plane, the lateral field of view (*L*) for OC-OCT can be determined based on the size of sensor array (L_{sensor}), and the magnification (M=11) from the sample plane and sensor plane (Equation (4.8)). For OC-OCT imaging based on 20X Olympus microscopic objectives (9mm effective focal length), a magnification of 11 from the sample plane to the camera sensor plane (5.5mm by 5.5mm), the lateral FOV is approximately 0.5mm (x) by 0.5mm (y).

$$L = \frac{L_{sensor}}{M} \tag{4.8}$$

The theoretical axial field of view determined by spectral sampling is approximately 1.2mm. The continuous interferometric spectrum can be expressed as Equation (4.9). On the other hand, the SLM projects a discrete modulation pattern: $e^{j\frac{2\pi kn}{N}}$ where *k* is the index of SLM pixel in a row and *N* is the total number of pixels in the row. Due to the sampling of wavenumber, $k = \left(\frac{2\pi}{\lambda} - \frac{2\pi}{\lambda_0}\right)/\delta k$ where $\delta k = \frac{2\pi\delta\lambda}{\lambda_0^2}$ is the interval of wavenumber sampled by SLM pixels. The discrete modulation pattern can thus be re-written as Equation (4.10). By correlating Equation (4.9) and Equation (4.10), the axial imaging range can be estimated using Equation (4.11). It is noted that the discrete signal cannot have a frequency larger than π. Hence the maximum value of *n* is N/2. In addition, wavelength sampling interval $\delta\lambda = \frac{d_0 L cos\theta}{F} \approx 0.094nm$. With groove width of the grating d_0 =1mm/600 and the pixel width of the SLM *L*=20µn, $\delta\lambda$ is estimated to be $0.094nm$. Accordingly, the theoretical axial imaging range is 1.2mm.

$$S(z) = ve^{j\left(\frac{2\pi}{\lambda} - \frac{2\pi}{\lambda_0}\right)z} \tag{4.9}$$

$$S_k = e^{j\left(\frac{2\pi}{\lambda} - \frac{2\pi}{\lambda_0}\right)\frac{n\lambda_0^2}{N\delta\lambda}} \tag{4.10}$$

$$z = \frac{n\lambda_0^2}{N\delta\lambda} \tag{4.11}$$

The above analysis gives the depth range in which OCT signal can be acquired. However, the imaging depth into a scattering sample is much smaller due to factors including sensitivity roll off and signal attenuation.

Another key parameter to describe system performance is the sensitivity. The theoretical sensitivity of the OC-OCT system is be estimated following a classical approach. Assume the detection is shot noise limited. The OCT signal magnitude (S_{OCT}) can be expressed as Equation (4.12) in which τ is exposure time, ρ is spectrometer efficiency, η denotes the detector quantum efficiency, h is the Planck constant, ν_0 is the center frequency of the light source spectrum, N is the number of pixels and P_0 is the output power of the light source. The shot noise variance can be expressed as Equation (4.13), and the signal to noise ratio (SNR) is estimated using Equation (4.14). Given $R_r >> R_s$ and the camera exposure time is adjusted to almost saturate the detector, Equation (4.14) can be re-written as Equation (4.15). The maximum number of photons detected is N_{max} as shown in Equation (4.16). Therefore, the SNR could be represented in Equation (4.17). According to R. Leitgeb et al, the sensitivity (ε) is the reciprocal of the sample reflectivity when SNR=1, as shown in Equation (4.18) where $N_{max}=5000$ is the number of photons that saturates individual pixels of the camera. The sensitivity of the imaging system is 73dB with $R_r=1$ and is 87dB with $R_r=4\%$.

$$S_{OCT} = \frac{\rho\eta\tau P_0}{Nh\upsilon_0}\sqrt{R_r R_s} \tag{4.12}$$

$$\sigma_{shot}^2 = \frac{\rho\eta\tau P_0}{N^2 h\upsilon_0}(R_r + R_s) \tag{4.13}$$

$$SNR = \frac{\langle S_{OCT}^2 \rangle}{\sigma_{shot}^2} = \frac{\rho\eta\tau P_0}{h\upsilon_0}\frac{R_r R_s}{R_r + R_s} \tag{4.14}$$

$$SNR = \frac{\langle S_{OCT}^2 \rangle}{\sigma_{shot}^2} = \frac{\rho\eta\tau P_0}{h\upsilon_0} R_s \tag{4.15}$$

$$N_{max} = (\frac{\rho\eta\tau P_0}{h\upsilon_0}/4)R_r \tag{4.16}$$

$$SNR = 4N_{max}R_s/R_r \tag{4.17}$$

$$\varepsilon = \frac{1}{R_s} = \frac{4NN_{max}}{R_r} \tag{4.18}$$

4.5 Comparison with Existing Technologies

OC-OCT provides a novel approach to address specific coordinate in 3D space for OCT imaging. By projecting Fourier basis functions by the SLM, OC-OCT can perform 2D parallel detection of signal from a specific depth (if the same Fourier basis function is utilized) or depths (if different Fourier basis function is utilized). In our OC-OCT system with the camera operated at 340 fps, it is feasible to achieve a smallest sampling interval of 3ms for enface imaging with 1000 by 1000 pixels. On the other hand, the spectral domain (SD) and swept source (SS) OCT systems in our lab takes 100k A-scans per second and the speed is comparable with most OCT systems used in research labs. With raster scanning, the SD and SS OCT systems have to acquire the entire 3D volume to generate an enface image. Hence it takes 10 seconds to generate an enface image. Therefore, OC-OCT has the potential to improve the imaging speed within enface plane by three orders of magnitude. Notably, this improvement is not achieved by reducing the time needed to acquire each pixel, but is achieved by directly addressing the pixel of interest.

The major contribution of this dissertation study is the development of innovative technologies to address limitations of raster beam scanning in conventional OCT imaging.

In addition to the generate technical advancements mentioned previously, comparison between our technology with several studies is presented.

(1) W. Zhang et al, describes an optically computed OCT imaging system (Figure 4.8). It uses the arbitrary waveform generator to generate optical signal with its amplitude modulated to be a cos(t^2). The modulated source signal then passes through a normal OCT Michaelson interferometer system. At the detector, an A-scan data processed by optical computed Fourier transformation system is detected.

The imaging system shown in Figure 4.8 performs A-scan through optical computation through the use of AWG modulated light source. However, the system still requires mechanical devices to help capture 2D images or 3D volumetric data. The significant advantage of OC-OCT developed in this dissertation study is its capability to address pixel in 3D space without mechanical scanning. This results in a simple and stable sample arm that has the potential to enable better spatiotemporal resolution.

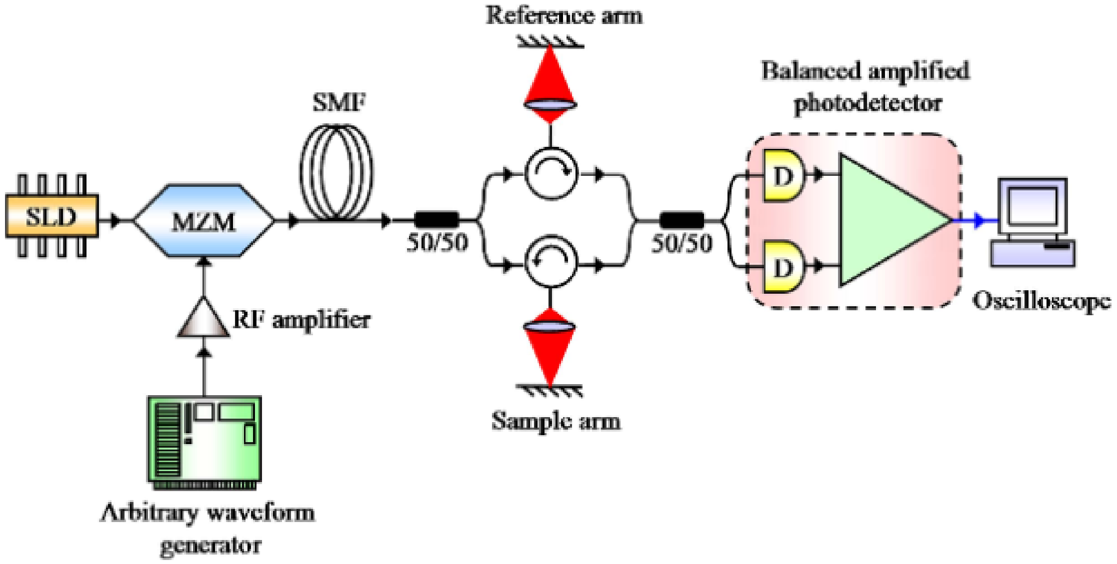

Figure 4.8, AWG for light modulation in optically computed OCT imaging.

Source: [63]

(2) Branislav Grajciar et al, developed a parallel spectral domain OCT system (Figure 4.9) that uses a cylindrical lens to generate line field illumination. The line illumination can be viewed as a set of parallel channels, each of them associated with a different lateral position on the sample. These channels are spectrally dispersed by the diffraction grating and recorded individually on different rows of the CCD area. Line field OCT system shown in Figure 4.9, eliminates the need of mechanical scanning for 2D B-scan. However, it still requires mechanical scanning for volumetric imaging. The line-field Fourier domain OCT technology developed in this dissertation study utilizes a similar mechanism for parallel imaging. However, our imaging system uses a programmable spatial light modulator to generate an arbitrary line field for parallel OCT imaging. It also scans the line field at the spatial light modulator for volumetric imaging.

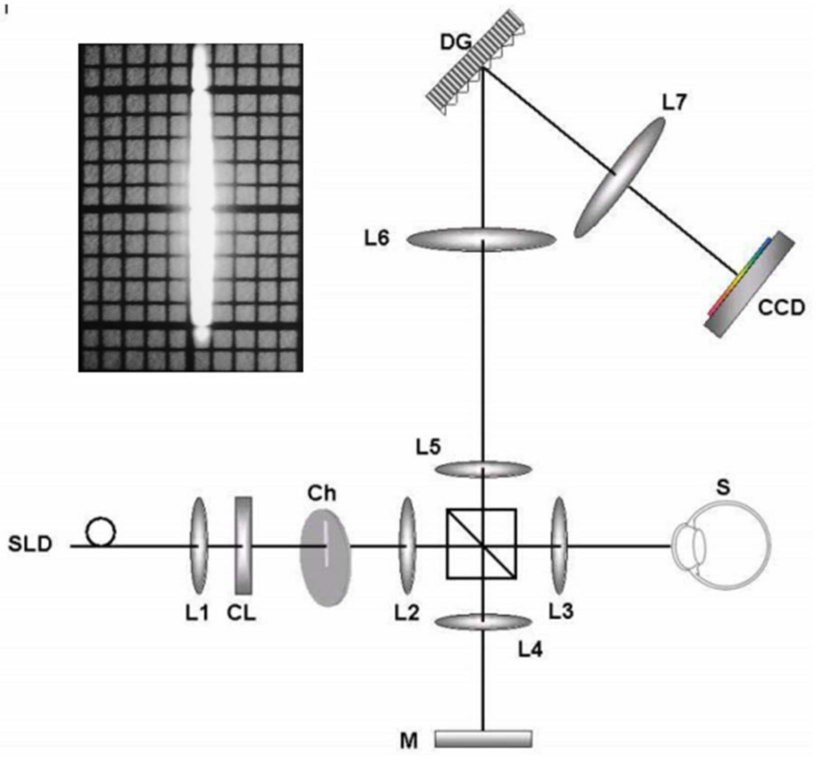

Figure 4.9, Spectral domain parallel OCT system.

Source: [62].

(3) S. Lee et al, developed a line-field OCT use a swept source and a line CCD camera (Figure 4.10) instead of the field CCD and spectrometer. It generates an elliptical beam onto a sample by using a cylindrical lens, and detects the wavelength-resolved interference signal using a line CCD camera. The sample is mechanically translated by a linear stage to generate volumetric image. Our technologies (OC-OCT and LF-FDOCT) completely remove the need for mechanical scanning device in 2D and 3D volumetric imaging. The imaging result of an arbitrary plane is not only fast but also more stable, because there is no movement through the whole process.

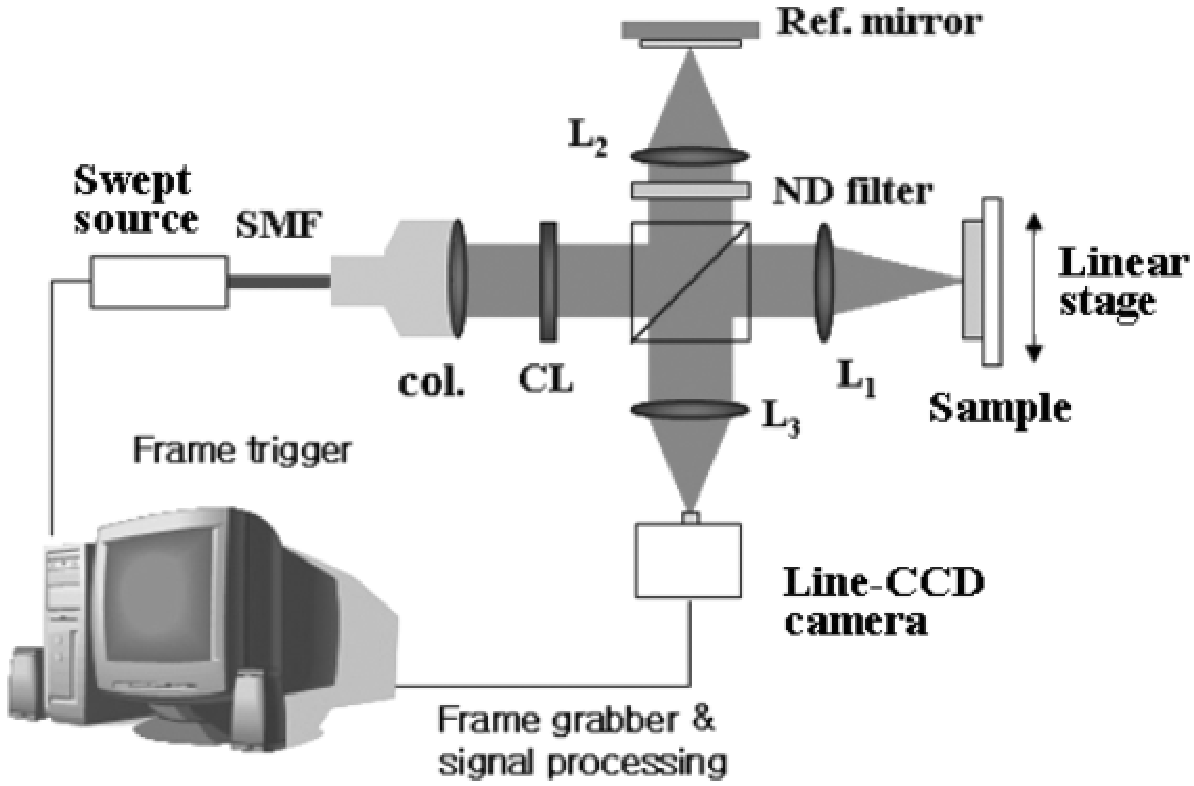

Figure 4.10, Line-Field Optical Coherence Tomography Using Frequency-Sweeping Source.

Source: [64]

4.6 Conclusion and Discussion.

The OC-OCT system described in this section enabled optically computed 3D OCT imaging for the first time to the best of our knowledge. OC-OCT is fundamentally different from existing technologies that take transverse plane as the preferential scanning dimension. For optical coherence microscopy (OCM) and full field OCT, mechanical scanning cannot be eliminated [62] [63] [64] [65]. For structural OCT imaging, the real and imaginary parts of complex OCT signal are measured with the SLM generating cosine and sine modulations and calculated the amplitude of OCT signal. The current OC-OCT system generated temporally interlace cosine and sine patterns for spectral modulation. Hence, its imaging speed was limited by the speed of the SLM (60Hz refreshing rate). Dispersion mismatch can also be compensated through optical computation by introducing a nonlinear phase term to the Fourier basis projected by the SLM. To fully utilize the speed of the camera, complex modulation of interferometric spectrum can also be achieved by projecting spatially interlaced cosine and sine patterns to the SLM. As discussed above, the small dynamic range of the camera (N_{max}) for parallel detection limits the sensitivity of OC-OCT. The sensitivity of our OC-OCT system is estimated to be 87dB, limited by the small dynamic range of the camera.

CHAPTER 5

LINE FIELD FOURIER DOMAIN OCT BASED ON A SPATIAL LIGHT

5.1 Introduction

Currently, in most implementations of OCT imaging, the broadband light output from a single mode fiber is focused to a point at the sample [55]. The light beam is steered mechanically in the transverse plane to generate B-scan or C-scan images. With a high-speed detector, it on average takes an extremely short period of time to acquire OCT data from one voxel from 3D space [57]. However, the spatiotemporal resolution of OCT imaging has been limited because of the raster scanning protocol utilized to acquire data in 3D space. The inter-Bscan sampling interval is large, and the inter-Cscan sampling interval is even larger. Moreover, the use of a mechanical beam scanner such as a galvanometer or a micro-electromechanical system (MEMS) increases the dimension, cost and complexity of the sample arm for an OCT imaging system.

An alternative approach to achieve extended transverse field of view (FOV) in OCT imaging is through parallel imaging. A parallel OCT system, such as a full field OCT and a line field OCT, illuminates an extended FOV and detects optical signal using an array detector (area scan or line scan camera) [59][60]. Parallel OCT imaging eliminates mechanical beam scanning, and has the potential to reduce instrument footprint, improve system robustness, and achieve ultra-high imaging speed.

In this section, a novel line field Fourier domain OCT (LF-FDOCT) imaging technology is investigated based on a 2D spatial light modulator (SLM) [58]. In the LF-FDOCT system, line field illumination is achieved by generating a line pattern at the SLM and projecting the SLM plane to the sample and reference arm. Interferometric spectra from different transverse locations at the line field are detected in parallel using a 2D camera for B-scan imaging. By scanning the line field at the SLM, multiple B-scans can be obtained for 3D imaging. The use of SLM to perform transverse scanning in volumetric OCT imaging is highly innovative and has not been investigated before to the best of our knowledge.

In conventional OCT imaging, mechanical scanners perform raster scanning along specific dimensions that are determined by the configuration and geometry of the scanner. Our LF-FDOCT technology achieves line field illumination by the SLM. The programmable SLM used in LF-FDOCT allows the fast scanning axis of OCT imaging to be conveniently altered. Given limited data acquisition bandwidth, LF-FDOCT imaging has the capability to achieve high spatiotemporal resolution along preferred fast scanning direction for specific applications.

The focus of this study is to investigate LF-FDOCT that uses SLM to perform transverse scanning. SLM also allows the acquisition of OCT signals from a set of spatial locations that are not continuous [61]. For example, SLM can be used for structured illumination and point spread function optimization in OCT imaging, which will be investigated in our future study.

The rest of this chapter is organized as follows. The principle of LF-FDOCT imaging is first described Afterwards, we present experimental results and conclude the chapter with discussions.

5.2 Principle of LF-FDOCT imaging

The configuration of LF-FDOCT is illustrated in Figure 5.1 (a). an LED is used as the light source. The output of the LED goes through a polarization beam splitter (PBS), and is imaged to the SLM (Holoeye LC-R 720) through an achromatic doublet lens (L1, f=250mm). The broadband light is modulated by the SLM and deflected by the PBS to illuminate the Michelson interferometer. With the PBS, the light incident into the SLM and the light detected by the camera have orthogonal polarizations, which is needed to ensure a one-to-one mapping between the pixel value of the SLM and its light reflectivity. A line pattern is generated at the SLM. Pixels along the line have high reflectivity and other pixels have 0 reflectivity. The line field is split by a beam splitter (BS), and imaged to the sample and reference mirror via an achromatic doublet lens (f=75mm). As illustrated in Figure 5.1 (a), the dimension of line field extension is difined as x direction, the direction of light beam propagation as z, and the direction orthogonal to x-z plane as y. After the beam splitter (BS), the optical fields from sample arm and reference arm superimpose and the interferometric signal is dispersed by a diffraction grating (600lp/mm), as illustrated in Figure 5.1 (b). It is worth mentioning that the spatial mapping in x dimension is not altered by the grating. The dispersed light is detected by a CMOS camera (Basler acA2000), streamed to the computer via a frame grabber (NI1433, National Instruments) and processed by graphic processing units (Quadro P2000, Nvidia).

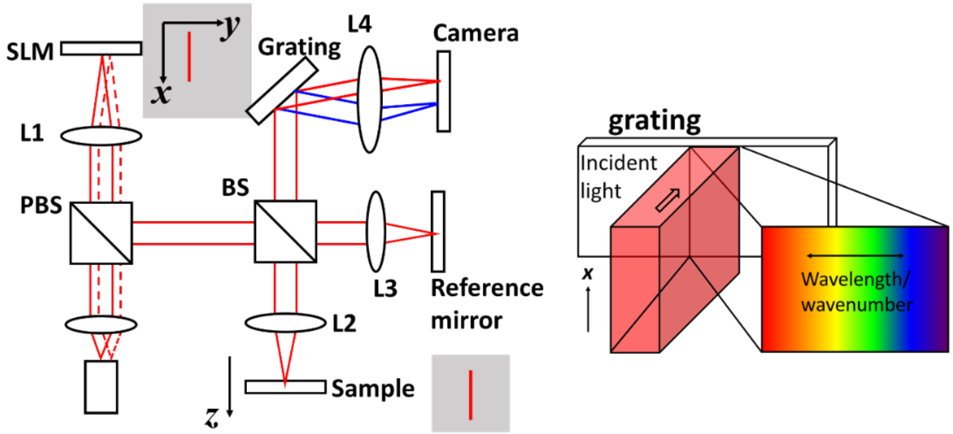

Figure.5.1 (a) The configuration of the LF-FDOCT system; (b) collimated interferometric light incidents into a grating and gets dispersed in a plane orthogonal to x direction. PBS: polarization beam splitter; SLM: spatial light modulator; BS: beam splitter; L1 –L4: achromatic doublet lenses (f=250mm, 75mm, 75mm and 100mm respectively).

The principle of line field FDOCT imaging is further illustrated in Figure 5.2 (a) and (b) show LF-OCT imaging with line field along x direction. Signal originating from a specific x coordinate (red box for x=xA) at the sample is mapped to its conjugate x coordinate in the camera sensor plane. Because of the dispersion introduced by the grating, light with different wavelength (or wavenumber k=2π/λ) is mapped to different pixels of the camera (red interferometric spectrum illustrated in Figure 5.2 (b)). Ideally, there is no crosstalk between channels at different transverse coordinates (red/green box at the sample plane corresponds to red/green interferometric spectrum at the camera plane). The camera is set such that each row of the pixels effectively detects a spectral interferogram originating from an x coordinate. An interferometric spectrum $S(k)_{x=x_0,y=y_0}$ is related to sample profile $I(z)_{x=x_0,y=y_0}$ through Fourier transform:$S(k)_{x=x_0,y=y_0} = \boldsymbol{F}\left[I(z)_{x=x_0,y=y_0}\right]$ where F indicates Fourier transform operator between z and k. To extract a 2D spatial domain OCT image, Fast Fourier transform (FFT) is applied to each row of data obtained from the camera after wavenumber linearization (wavelength to wavenumber interpolation). By varying the y coordinate of the line pattern at the SLM ($y=0$, Δy, $2\Delta y\ldots$), B-scans from different y coordinates are obtained to form a C-scan.

The programmable SLM also offers unique advantage of flexible choice of fast scanning dimension. As shown in Figure 5.2 (c), the SLM can generate line illumination that has an angle (α) with regard to the x axis of the Cartesian coordinate system. The spectral interferogram from an x coordinate (x_A or x_B) is then detected by camera pixels at the corresponding x coordinate without transverse crosstalk. As shown in Figure 5.2 (d), spectral interferograms from different points of the oblique line field are linearly shifted from one another at the detector plane (red and green spectra), because of the shift along y coordinate in the sample plane. However, spectral shift in Fourier domain does not affect the magnitude of spatial domain OCT signal, because spatial domain OCT signal is obtained by performing Fourier transform on Fourier domain measurement and spectral shifting in Fourier domain corresponds to a linear phase term in spatial domain signal. Using line field shown in Figure 5.2 (c), a B-scan can be obtained by performing FFT on the rows of data acquired by the camera. Similarly, C-scan can be obtained by scanning the line field in y dimension.

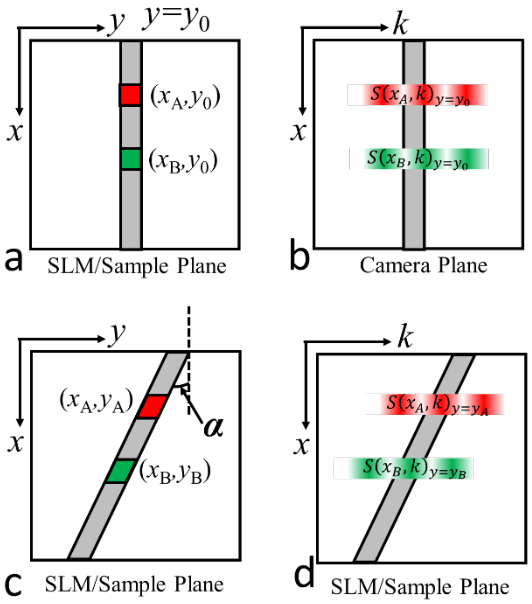

Figure 5.2. (a) line field illumination along *x* dimension; (b) spectral interferograms corresponding to line illumination along x axis; (c) line field illumination that has an angle α with regard to x axis; (d) spectral interferograms corresponding to line illumination that has an angle α with regard to x axis.

5.3 Results

The depth resolved imaging capability of the LF-FDOCT system has been validated. Line illumination along x axis is generated and imaged a mirror with an impulse reflectivity profile in axial dimension. To characterize the axial point spread function (PSF) of the imaging system, the interferometric spectra is acquired, and performed FFT on rows of data detected by the camera, and averaged A-scans obtained from x coordinates to generate the axial PSF. Before Fourier transform, pixel to wavenumber calibration is performed, because the camera did not sample the wavenumber uniformly. Consider the sample is illuminated by a line field at y=y0. After the grating, the wavenumber seen by the nth pixel of the camera is k0(n)=ay0+b+g(n) where the first two terms describe the global shifting of the spectrum dependent on y coordinate and g(n) describes the non-uniform sampling of wavenumber by camera pixels. To convert the measurement to wavenumber domain, k0(n) is calibrated by linearizing the phase extracted from interferometric spectrum and performed FFT on k linearized spectral data. Axial PSFs obtained without and with wavenumber linearization are shown in Figure 5.3 (a), as solid curves in red and in black. Gaussian fitting is used to obtain the results and extracts the axial resolution was estimated to be 11 µm. It is clear that wavenumber linearization is essential to preserve the axial resolution of FDOCT imaging. Theoretically, the above described wavenumber calibration and interpolation process is only valid for line field at y=y0. For a line field at a different y coordinate, the camera sees shifted interferometric spectra: k(n)= k0(n)+a(y-y0). The wavenumber calibration performed for line field at y0 can be used to linearize wavenumber for other y coordinates, because the global shifting in Fourier domain (α(y-y0)) corresponds to a linear phase modulation term in spatial domain OCT signal after Fourier transform, and does not affect the magnitude of OCT signal. To validate this, pixels of the SLM are selected to generate line field illumination at y=-0.2mm, -0.1mm, 0, 0.1mm and 0.2mm at the sample plane and obtained axial PSFs shown in Figure 5.3 (b). The PSF is fit with a Gaussian function and quantified the axial resolution of OCT using the full width half maximum (FWHM) of the Gaussian function. As shown in Figure 5.3 (c), axial resolution remained consistent for line field at different y coordinate, using the same wavenumber calibration.

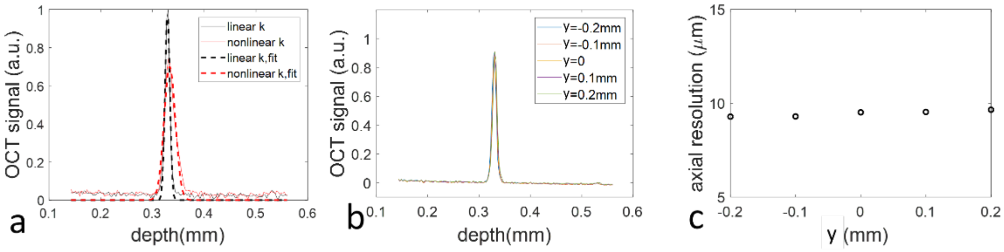

Figure 5.3. (a) Experimental axial PSFs obtained without (solid, red) and with (solid, black) wavenumber linearization, and Gaussian fittings of the PSFs (dashed curves); (b) experimental axial PSFs obtained with line field illumination at y=-

0.2mm, -0.1mm, 0, 0.1mm and 0.2mm; (c) axial resolution for line field illumination at y=-0.2mm, -0.1mm, 0, 0.1mm and 0.2mm.

The lateral resolution of LF-FDOCT is validated by imaging a variable line grating resolution target. Different regions of the resolution target are imaged with increasing line density (line pairs per millimeter, lp/mm). Figure 5.4 (a) (b) were obtained from regions with 50lp/mm patterns and 100 lp/mm. 50 lp/mm is the highest density that the LF-FDOCT system can resolve, suggesting a lateral resolution of 20µm. Figure 5.4 (b) was obtained from the line pattern at a density of 100 lp/mm and the structure was no longer resolvable in LF-FDOCT.

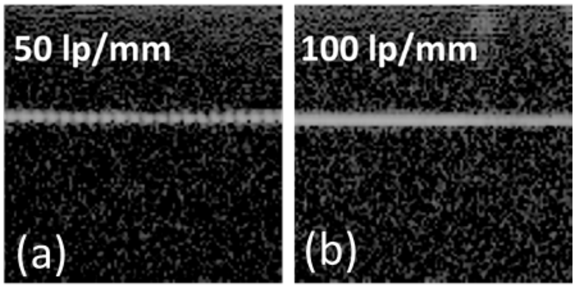

Figure 5.4. B-scan image obtained with LF-FDOCT from the variable line grating resolution target at a region with (a) 50 lp/mm pattern; (b) 100 lp/mm pattern.

Flexible selection of fast scanning dimension is demonstrated with LF-FDOCT. As illustrated in Figure 5.5 (a), a region of the variable line grating resolution target is imaged and the SLM is programmed to generate a series of line fields for illumination. The first line field was along x direction. Subsequent line patterns had larger angles ($\alpha i=(i-1)\alpha 0$ for the ith line pattern) with regard to the x axis of the Cartesian coordinate. The first line field acquired signal from a region with uniform reflectivity. Hence the LF-FDOCT image obtained (Figure 5.5 (b)) shows a uniform signal magnitude along x direction. For the 2nd line field ($\alpha=\alpha 0$), the left part of the line acquired OCT signal from a region with constant reflectivity and the right part of the line acquired OCT signal from a region with periodical reflectivity pattern, as shown in Figure 5.5 (c). When illuminated by the 3rd to 6th line pattern, the LF-FDOCT image shows an increasingly larger portion obtained from the region with alternating reflectivity (Figure 5.5 (d)-(g)). This is consistent with the geometry shown in Figure 5.5 (a).

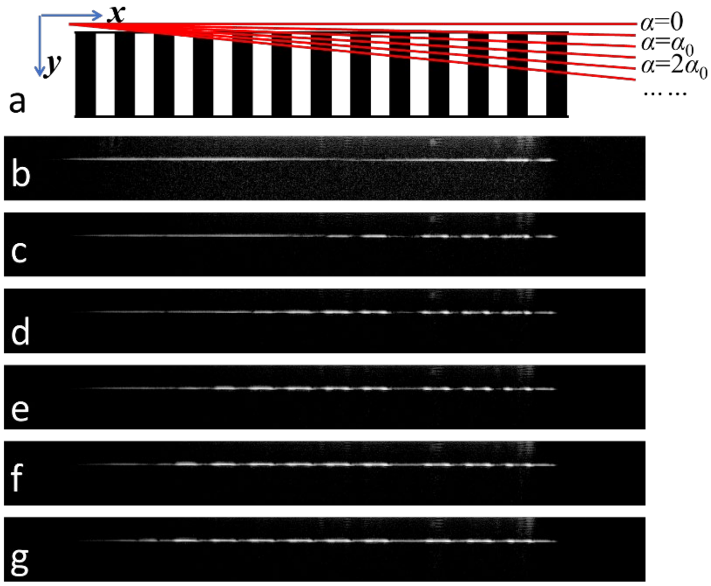

Figure 5.5. (a) SLM generated patterns that had an angle with regard to x axis: $\alpha_i=(i-1)\alpha_0$ for the i^{th} line fields; (b) –(g) 2D images obtained from the 1^{st} to the 6^{th} line fields.

3D imaging capability of LF-FDOCT is demonstrated along different fast scanning directions. A 3D phantom made by depositing photoresist layer (SU-8 2035) with 37μm elevation on silicon substrate using photolithography facility is imaged. An area with checker patterns is first imaged. Line field along x direction is generated and a B-scan ($I(x,z)_{y=y_0}$) is acquired at the corresponding y coordinate ($y=y_0$). By scanning the line field along y direction (Figure 5.6 (a)), B-scans from different y coordinates are obtained to generate a 3D data set ($I(x,y,z)$). From the 3D data set acquired, signal along z axis is averaged and the *en-face* image is generated showing the checker pattern in Figure 5.6 (b). In Figure 6 (c) and (d), 2D cross-sectional images obtained along the dashed lines is shown in Figure 5.6 (b). On the other hand, the same 3D phantom is imaged using a different set of line fields along axis x’ as illustrated in Figure 5.6 (e). With these line fields, the transverse plane is scanned for volumetric imaging. Signal along z axis is averaged and the *en-face* image is generated shown in Figure 5.6 (f). B-scans corresponding to the dashed lines in Figure 5.6 (f) are shown in Figure 5.6 (g) and (h). Figure 5.6 (f) appears to be a sheared version of Figure 5.6 (b). This is because the line fields in Figure 5.6 (e) effectively samples the pixels in spatial coordinate x’-h and $\begin{bmatrix} x' \\ h \end{bmatrix} = \begin{bmatrix} cos(\alpha) & -sin(\alpha) \\ 0 & 1 \end{bmatrix} \begin{bmatrix} x \\ y \end{bmatrix} = \boldsymbol{\phi} \begin{bmatrix} x \\ y \end{bmatrix}$ (Figure 5.6 (i)). With the coordinate transformation matrix $\boldsymbol{\phi}$, image shown in Figure 5.6 (f) is converted to Cartesian coordinate ϕ and the image is shown in Figure 5.6 (j) that is consistent with Figure 5.6 (b). The 3D phantom at a region with the pattern of “NJIT” is also imaged. Line scanning is performed using the pattern shown in Figure 5.6 (a) and acquired the volumetric data set. 3D rendering of the volumetric data is shown in Figure 5.7. The area under the letters is dark because of light attenuation.

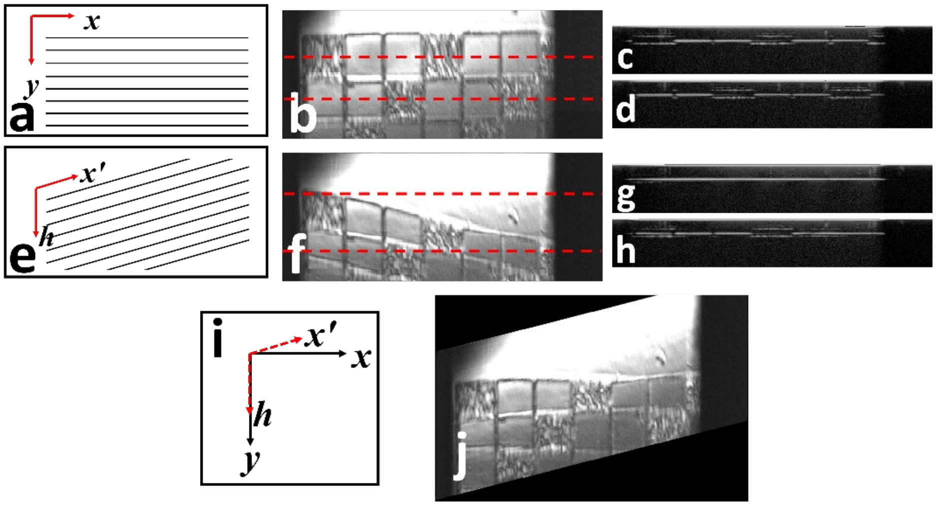

Figure 5.6. (a) SLM scanning patterns that samples the pixels in the coordinate system of x-y; (b) *en-face* image of the checker pattern obtained using scanning pattern shown in Figure 5.6 (a); (c) and (d) 2D cross-sectional images along the dashed lines in Figure 5.6 (b); (e) SLM scanning patterns that samples the pixels in the coordinate system of x’-h; (b) *en-face* image of the checker pattern obtained using scanning pattern shown in Figure 5.6 (e); (g) and (h) 2D cross-sectional

images along the dashed lines in Figure 5.6 (e); (i) coordinate system x’-h is a rotated version of x-y; (j) *En-face* image converted to coordinate system x-y from measurement based on coordinate system x’-h.

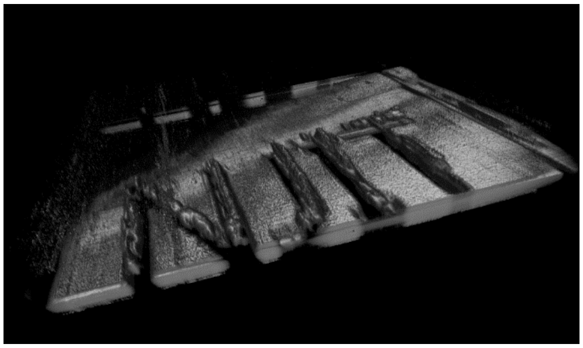

Figure 5.7. 3D render volumetric data showing the pattern of “NJIT”.

LF-FDOCT imaging on scattering samples is further demonstrated. A phantom is made by stacking three layers of scotch tape together. The B-scan obtained from LF-FDOCT is shown in Figure 5.8 (a). Onion cells is also imaged using the LF-FDOCT system. Individual onion cells can be identified in Figure 5.8 (b).

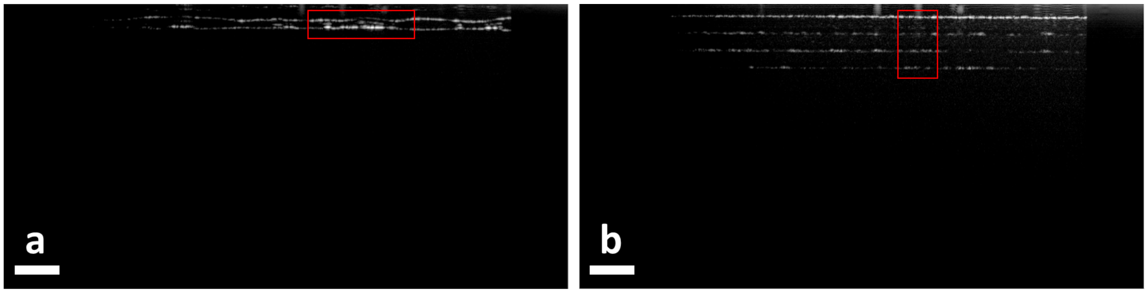

Figure 5.8 (a) cross-sectional image of onion cells; (b) cross-sectional image of three layers of scotch tape layer; The white bar indicates 100 μm.

5.4 Conclusion and Discussion

In this research, line field Fourier domain OCT system using an SLM for lateral scanning and uses a 2D camera for parallel signal detection has been developed and validated. Imaging experiments have been performed to demonstrate the cross-sectional imaging capability of the LF-FDOCT system. It is known that the signal quality of a parallel OCT imaging system can be affected by the cross-talk between different transverse signal channels. For turbid sample, photons scattered by a particle at pixel with lateral coordinate xA (Figure 5.2(a)) may undergo multiple scattering events and reach transverse coordinate xB at the camera. If coherence is still preserved, these multiply scattered photons contribute to signal that is misinterpreted in the origin of lateral and axial coordinate. If coherence is not preserved, multiply scattered photons generate a noise flood and reduce the effective dynamic range of the detector. Conventional OCT system based on fiber-optic interferometry and pointwise scanning can effectively suppress multiple scattering through confocal gating. Compared to other implementations of parallel OCT imaging, the LF-FDOCT system can be conveniently modified to effectively suppress the contribution of multiple scattering.

CHAPTER 6

SUMMARY AND FUTURE WORK

6.1 Summary

In this dissertation research, innovative technologies were developed to address limitations of raster beam scanning in conventional OCT imaging. Novel methods to address specific coordinate in 3D space were utilized in scanless OCT imaging.

Chapter 2 describes the principle and applications of OCT technology.

Chapter 3 describes scanning strategies utilized in conventional OCT imaging and their limitations. In conventional OCT imaging, raster scanning is performed to address different spatial locations within the 3D space. It requires a mechanical scanner to steer the light beam and results in limited spatiotemporal resolution in OCT imaging.

Chapter 4 describes an innovative optically computed optical coherence tomography (OC-OCT) technology that addresses spatial location through optical computation. The OC-OCT system performs depth resolved imaging by computing the Fourier transform of the interferometric spectra optically. The OC-OCT system modulates the interferometric spectra with Fourier basis function projected to a spatial light modulator and detects the modulated signal without spectral discrimination. The novel optical computation strategy enables volumetric OCT imaging without performing mechanical scanning and without the need for Fourier transform in a computer. The principle of OC-OCT imaging system is presented. The effectiveness of the system is validated using experimental results.

Chapter 5 describes a line field (LF) Fourier domain optical coherence tomography (FDOCT) system that addresses spatial location by scanning a line field electronically with a spatial light modulator. The LF-FDOCT system performs lateral scanning using a two-dimension spatial light modulator and performs parallel signal detection using a two-dimensional sensor (CMOS camera). The LF-FDOCT system allows parallel acquisition of OCT signal from an entire cross-sectional 2-D image (B-scan) and offers flexibility to select arbitrary fast scanning dimension. The principle of LF-FDOCT imaging are demonstrated. Experimental results are obtained from the LF-FDOCT imaging system.

6.2 Future Work

In conclusion, by investigating novel methods to address 3D spatial locations in OCT imaging, this dissertation study provides solutions to overcome the limitation of conventional raster scanning approach in OCT imaging. Future development will involve technological advancement and the application of scanless OCT imaging to study different dynamic events for biomedical research.

The OC-OCT technology allows flexible data acquisition within an oblique plane by projecting different Fourier basis to different SLM rows. In this dissertation, 3D imaging was acquired by projecting the same Fourier basis function to different rows of the SLM and sequentially acquiring en face images at different depths. In the future, if fast imaging is needed in an oblique plane, the OC-OCT system can project different Fourier basis functions to different rows of the SLM and make the oblique plane the dimension of preferential data acquisition. In addition, OC-OCT captures the real and imaginary part of complex OCT signal, by projecting cosine and sine patterns through the SLM to generate structural OCT image. This implies the technology can be directly used for phase resolved imaging that is sensitive to nanometer scale displacement. This suggests OC-OCT's applications in optical coherence elastography and imaging study of cell dynamics. Initial results of phase resolved OC-OCT imaging was reported in our recent conference paper (Optical computation for complex OCT, OSA Biophotonics Congress: Biomedical Optics, OTu1E.5). In the future, a systematic study can be conducted to validate and optimize phase resolved OC-OCT imaging. Current OC-OCT system generates temporally interlace cosine and sine patterns for spectral modulation. Hence, its imaging speed was limited by the speed of the SLM (60Hz refreshing rate). Complex modulation of interferometric spectrum can also be achieved by projecting spatially interlaced cosine and sine patterns to the SLM. The pattern is temporally stationary. This will allow the imaging system to fully utilize the bandwidth of the camera.

OC-OCT is essentially a parallel imaging technique. Hence, the imaging quality is affected by lateral cross-talk. However, SLM can be conveniently programmed to perform structured illumination and suppress lateral cross talk. For example, we can selectively activate a discontinuous set of SLM rows and take measurements at corresponding locations to reject multiply scattered photons. The entire field of view can be covered by repeating the above process with different areas illuminated.

For LF-FDOCT system, the LF-FDOCT system has the potential to be modified to effectively suppress the contribution of multiple scattering. As mentioned above, the SLM can be programmed to enable a discontinuous set of pixels along the illumination line field. A digital confocal mechanism can be achieved by detecting signals only at these pixels. A Bscan image can be assembled using measurements obtained under different illumination patterns. Moreover, LFOCT allows an asymmetric optical configuration for illumination and detection. This facilitates parallel measurement of complex output from a series of point illuminations and full reconstruction of scattering field of the sample.

REFERENCES

[1] A. Wax, and V. Backman, "Classical light scattering models," in Biomedical applications of light scattering, NY, USA: McGraw- Hill, 2010, pp. 3 – 29.

[2] W. F. Cheong, S. A. Prahl, and A. J. Welch, "A review of the optical properties of biological tissues," IEEE Journal of Quantum Electronics, vol. 26, no. 12, pp. 2166-2185, 1990.

[3] E. A. Swanson, J. A. Izatt, M. R. Hee, D. Huang, C. P. Lin, J. S. Schuman, C. A. Puliafito, and J. G. Fujimoto, "In vivo retinal imaging by optical coherence tomography," Optics Letters, vol. 18, pp. 1864-1866, 1993.

[4] N. Nassif, B. Cense, B. H. Park, S. H. Yun, T. C. Chen, B. E. Bouma, G. J. Tearney, and J. F. de Boer, "In vivo human retinal imaging by ultrahigh-speed spectral domain optical coherence tomography," Optics Letters, vol. 29, pp. 480-482, 2004.

[5] M. Wojtkowski, R. Leitgeb, A. Kowalczyk, T. Bajraszewski, and A. F. Fercher, "In vivo human retinal imaging by fourier domain optical coherence tomography," Journal of Biomedical Optics, vol. 7, pp. 457–463, 2002.

[6] D. Huang, E. A. Swanson, C. P. Lin, J. S. Schuman, W. G. Stinson, W. Chang, M. R. Hee, T. Flotte, K. Gregory, and C. A. Puliafito, "Optical coherence tomography," Science, vol. 254, no. 5035, pp. 1178–1181, 1991.

[7] O. Raffel, T. Akasaka, I. Jang. 2008. "Cardiac optical coherence tomography." Heart 94:1200–1210, 2008

[8] W. Drexler, M. Liu, A. Kumar, T. Kamali, A. Unterhuber, and R. A. Leitgeb, "Optical coherence tomography today: speed, contrast, and multimodality," Journal of Biomed. Optics, vol. 19, no. 7, 2014.

[9] P. Bouguer, Essai d'optique sur la gradation de la lumière [Optics essay on the attenuation of light] (in French). Paris, France: Claude Jombert. pp. 16–22. 1729.

[10] A. Weymouth, "Optical coherence tomography of ocular diseases 3rdEdition by schuman JS, puliafito CA, fujimoto JG and duker JS thorofare, New Jersey, USA: slack Inc, 2013 615 pages RRP $358.84," Clinical and Experimental Optometry, vol. 97, no. 2, p. 192, 2014.

[11] A. Fercher, C. Hitzenberger, W. Drexler, G. Kamp, H. Sattmann. In Vivo Optical Coherence Tomography. Am Journal Ophthal 1993; 116:113–4.

[12] E. A. Swanson, J. A. Izatt, M. R. Hee, D. Huang, C. P. Lin, J. S. Schuman, C. A. Puliafito, and J. G. Fujimoto, "In vivo retinal imaging by optical coherence tomography," Opt. Lett. 18, 1864-1866, 1993

[13] C. Puliafito, M. Hee, C. Lin, E. Reichel, J. Schuman, J. Duker, et al, “Imaging of macular diseases with optical coherence tomography”. Ophthalmology 1995; 102:217–29.

[14] M. Wojtkowski, V. Srinivasan, T. Ko, J. Fujimoto, A. Kowalczyk, J. Duker. “Ultrahigh-resolution, high-speed, Fourier domain optical coherence tomography and methods for dispersion compensation”. Opt Exp 2004; 12:2404–22.

[15] E. Ergun, B. Hermann, M. Wirtitsch, A. Unterhuber, T. Ko, H. Sattmann, et al, “Assessment of central visual function in Stargardt’s disease/fundus flavimaculatus with ultrahigh-resolution optical coherence tomography.” Investigative Ophthalmology & Visual Science 2005; 46:310–6.

[16] W. Drexler, H. Sattmann, B. Hermann, T. Ko, M. Stur, A. Unterhuber, et al, “Enhanced visualization of macular pathology with the use of ultrahigh-resolution optical coherence tomography.” Archives of Ophthalmology 2003; 121:695–706.

[17] M. Wirtitsch, E. Ergun, B. Hermann, A. Unterhuber, M. Stur, C. Scholda, et al, “Ultrahigh resolution optical coherence tomography in macular dystrophy”. Am J Ophthalmol 2005; 140:976–83.

[18] G. Wollstein, L. Paunescu, T. Ko, J. Fujimoto, A. Kowalevicz, I. Hartl, et al, “Ultrahigh-resolution optical coherence tomography in glaucoma.” Ophthalmology 2005; 112:229–37.

[19] M. Menke, P. Knecht, V. Sturm, S. Dabov, J. Funk. “Reproducibility of Nerve Fiber Layer Thickness Measurements Using 3D Fourier-Domain OCT.” Investigative Ophthalmology & Visual Science 2008;49:5386–91.

[20] I. Jang, B. Bouma, D. Kang, S. Park, S. Park, K. Seung, K. Choi, M. Shishkov, K. Schlendorf, E. Pomerantsev, S. Houser, H. Aretz, and G. Tearney, “Visualization of coronary atherosclerotic plaques in patients using optical coherence tomography: comparison with intravascular ultrasound,” J. Am. Coll. Cardiol. 39_4_, 604–609 2002.

[21] B. Bouma and G. Tearney, “Clinical imaging with optical coherence tomography,” Acad. Radiol. 98, 942–953 2002.

[22] B. Bouma, G. Tearney, H. Yabushita, M. Shishkov, C. Kauffman, D. DeJoseph Gauthier, B. MacNeill, S. Houser, H. Aretz, E. Halpern, and I. Jang, “Evaluation of intracoronary stenting by intravascular optical coherence tomography,” Heart 893, 317–320 2003.

[23] M. E. Brezinski, G. J. Tearney, B. E. Bouma, J. A. Izatt, M. R. Hee, E. A. Swanson, J. F. Southern, and J. G. Fujimoto, “Optical coherence tomography for optical biopsy: Properties and demonstration of vascular pathology,” Circulation 936, 1206–1213 1996.

[24] M. E. Brezinski, G. J. Tearney, B. E. Bouma, S. A. Boppart, M. R. Hee, E. A. Swanson, J. F. Southern, and J. G. Fujimoto, “Imaging of coronary artery microstructure in vitro with optical coherence tomography,” Am. J. Cardiol. 771, 92–93 1996.

[25] M. E. Brezinski, G. J. Tearney, N. J. Weissman, S. A. Boppart, B. E. Bouma, M. R. Hee, A. E. Weyman, E. A. Swanson, J. F. Southern, and J. G. Fujimoto, “Assessing atherosclerotic plaque morphology: comparison of optical coherence tomography and high frequency intravascular ultrasound,” Heart 775, 397–403 1997.

[26] A. H. Chau, R. C. Chan, M. Shishkov, B. MacNeill, N. Iftimia, G. J. Tearney, R. D. Kamm, B. E. Bouma, and M. R. Kaazempur-Mofrad, “Mechanical analysis of atherosclerotic plaques based on optical coherence tomography,” Ann. Biomed. Eng. 3211, 1494–1503 2004.

[27] G. J. Tearney, M. E. Brezinski, S. A. Boppart, B. E. Bouma, N. Weissman, J. F. Southern, E. A. Swanson, and J. G. Fujimoto, “Catheter-based optical imaging of a human coronary artery,” Circulation 9411, 3013 1996.

[28] A. F. Zuluaga and B. E. Bouma, Multi-channel optical coupler for spinning catheter, U.S. Patent No. 6,895,137 2005.

[29] S. A. Boppart, W. Luo, D. L. Marks, and K. W. Singletary, “Optical coherence tomography: feasibility for basic research and imageguided surgery of breast cancer,” Breast Cancer Res. Treat. 842, 85–97 2004.

[30] A. M. Zysk and S. A. Boppart, “Computational methods for analysis of human breast tumor tissue in optical coherence tomography images,” J. Biomed. Opt. 115, 054015 2006.

[31] D. Cao, C. Lin, S. H. Woo, R. Vang, T. N. Tsangaris, and P. Argani, “Separate cavity margin sampling at the time of initial breast lumpectomy significantly reduces the need for reexcisions,” Am. J. Surg. Pathol. 2912, 1625–1632 2005.

[32] F. T. Nguyen, A. M. Zysk, J. G. Kotynek, F. J. Bellafiore, K. M. Rowland, P. A. Johnson, E. J. Chaney, and S. A. Boppart, “Portable real-time optical coherence tomography system for intraoperative imaging and staging of breast cancer,” Proc. SPIE 6430, 64300H 2007.

[33] E. Glenn. "Electromagnetic Waves". The Physics Hypertextbook. Retrieved 4 June

2018.

[34] "The Impact of James Clerk Maxwell's Work". www.clerkmaxwellfoundation.org. Archived from the original on 17 September 2017. Retrieved 4 September 2017.

[35] X. Liu, Basil Hubbi, and Xianlian Zhou, "Spatial coordinate corrected motion tracking for optical coherence elastography," Biomed. Opt. Express 10, 6160-6171 (2019)

[36] Y. Jia, S. T. Bailey, D. J. Wilson, O. Tan, M. L. Klein, C. J. Flaxel, B. Potsaid, J. J. Liu, C. D. Lu, and M. F. Kraus, "Quantitative optical coherence tomography angiography of choroidal neovascularization in age-related macular degeneration," Ophthalmology 121, 1435-1444 2014.

[37] Y. Qiu, Y. Wang, Y. Xu, N. Chandra, J. Haorah, B. Hubbi, B. J. Pfister, and X. Liu, "Quantitative optical coherence elastography based on fiber-optic probe for in situ measurement of tissue mechanical properties," Biomedical Optics Express 7, 688-700 2016.

[38] T. Akkin, D. Landowne, and A. Sivaprakasam, "Detection of neural action potentials using optical coherence tomography: intensity and phase measurements with and without dyes," Frontiers in neuroenergetics 2, 22 2010.

[39] M. Wojtkowski, V. Srinivasan, J. G. Fujimoto, T. Ko, J. S. Schuman, A. Kowalczyk, and J. S. Duker, "Three-dimensional retinal imaging with high-speed ultrahigh-resolution optical coherence tomography," Ophthalmology 112, 1734-1746 2005.

[40] R. Leitgeb, C. K. Hitzenberger, and A. F. Fercher, "Performance of fourier domain vs. time domain optical coherence tomography," Opt. Express 11, 889-894 2003.

[41] M. A. Choma, M. V. Sarunic, C. Yang, and J. A. Izatt, "Sensitivity advantage of swept source and Fourier domain optical coherence tomography," Opt. Express 11, 2183-2189 2003.

[42] D. R. Solli and B. Jalali, "Analog optical computing," Nature Photonics 9, 704 2015.

[43] W. Zhang, X. Zhang, C. Wang, W. Liao, S. Ai, J. Hsieh, N. Zhang, and P. Xue, "Optical computing optical coherence tomography with conjugate suppression by dispersion," Opt. Lett. 44, 2077-2080 2019.

[44] C. Maurer, A. Jesacher, S. Bernet, M. Ritsch-Marte, Laser & Photonics Reviews. 5(1):81-101 2011.

[45] Z. Zhang, X. Ma, and J. Zhong, "Single-pixel imaging by means of Fourier spectrum acquisition," Nature Communications 6, 6225 2015.

[46] A. C. Boccara, F. Charbonnier, D. Fournier, and P. Gleyzes, ''D´etection analogique

multicanal,'' French patent FR90.092255 (June 29, 1990), and international extensions.

[47] P. Gleyzes, F. Guernet, and A. C. Boccara, J. Opt. (Paris) 26, 251 1995.

[48] P. Gleyzes, A. C. Boccara, and H. Saint-Jalmes, "Multichannel Nomarski microscope with polarization modulation: performance and applications," Opt. Lett. 22, 1529-1531, 1997.

[49] J. C. Canit and J. Badoz, "New design for a photoelastic modulator," Appl. Opt. 22, 592-594 (1983).

[50] L. Blanchot, M. Lebec, H. Saint-Jalmes, E. Beaurepaire, P. Gleyzes, and A. C. Boccara, to be presented at SPIE BiOS '98, January 24–30, San Jose, Calif.

[51] D. Huang, E. A. Swanson, C. P. Lin, J. S. Schuman, W. G. Stinson, W. Chang, M. R. Hee, T. Flotte, K. Gregory, and C. A. Puliafito, "Optical coherence tomography," science 254, 1178-1181 1991.

[52] M. Choma, M. Sarunic, C. Yang, and J. Izatt, "Sensitivity advantage of swept source and Fourier domain optical coherence tomography," Opt. Express 11(18), 2183–2189 2003.

[53] X. Liu, M. Balicki, R. H. Taylor, and J. U. Kang, "Towards automatic calibration of Fourier-Domain OCT for robot-assisted vitreoretinal surgery," Opt. Express 18, 24331-24343 2010.

[54] K. Gallo and G. Assanto, "All-optical diode based on second-harmonic generation in an asymmetric waveguide," J. Opt. Soc. Am. B 16(2), 267–269 1999.

[55] B. R. Masters, "Three-dimensional microscopic tomographic imagings of the cataract in a human lens in vivo," Opt. Express 3(9), 332–338 1998.

[56] D. Yelin, D. Oron, S. Thiberge, E. Moses, and Y. Silberberg, "Multiphoton plasmon-resonance microscopy," Opt. Express 11(12), 1385–1391 2003.

[57] B. N. Behnken, G. Karunasiri, D. R. Chamberlin, P. R Robrish, and J. Faist," Real-time imaging using a 2.8~THz quantum cascade laser and uncooled infrared microbolometer camera,"' Opt. Lett. 33(5), 440–442 2008.

[58] OptiXplorer Education Kit Manual. Holoeye Photonics AG, 2002

[59] D. J. Fechtig, B. Grajciar, T. Schmoll, C. Blatter, R. M. Werkmeister, W. Drexler, and R. A. Leitgeb, "Line-field parallel swept source MHz OCT for structural and functional retinal imaging," Biomed. Opt. Express 6, 716-735 2015

[60] E. Beaurepaire, A. C. Boccara, M. Lebec, L. Blanchot, and H. Saint-Jalmes, "Full-field optical coherence microscopy," Opt. Lett. 23, 244-246 1998

[61] Y. Wang, Q. Kang, Y. Zhang, and X. Liu, "Optically computed optical coherence tomography for volumetric imaging," Opt. Lett. 45, 1675-1678

[62] B. Grajciar, M. Pircher, A. F. Fercher, and R. A. Leitgeb, "Parallel Fourier domain optical coherence tomography for in vivo measurement of the human eye," Opt. Express 13, 1131-1137 2005

[63] X. Zhang, T. Huo, C. Wang, W. Liao, S. Ai, W. Zhang, J. Hsieh, P. Xue, “Optical computing for optical coherence tomography”. Scientific Reports. 6. 37286. 10.1038/srep37286. 2016

[64] S. Lee and B. Kim, "Line-Field Optical Coherence Tomography Using Frequency-Sweeping Source," in IEEE Journal of Selected Topics in Quantum Electronics, vol. 14, no. 1, pp. 50-55, Jan.-feb. 2008.

[65] C. Zevallos, O., Keller, B., Viehland, C. et al, Live volumetric (4D) visualization and guidance of in vivo human ophthalmic surgery with intraoperative optical coherence tomography. Sci Rep 6, 31689 2016.